

Solar neutrino flux at keV energies

Edoardo Vitagliano,^a Javier Redondo^{a,b} and Georg Raffelt^a

^aMax-Planck-Institut für Physik (Werner-Heisenberg-Institut),
Föhringer Ring 6, 80805 München, Germany

^bDepartment of Theoretical Physics, University of Zaragoza,
P. Cerbuna 12, 50009 Zaragoza, Spain

E-mail: edovita@mpp.mpg.de, jredondo@unizar.es, raffelt@mpp.mpg.de

Abstract. We calculate the solar neutrino and antineutrino flux in the keV energy range. The dominant thermal source processes are photo production ($\gamma e \rightarrow e\nu\bar{\nu}$), bremsstrahlung ($e + Ze \rightarrow Ze + e + \nu\bar{\nu}$), plasmon decay ($\gamma \rightarrow \nu\bar{\nu}$), and $\nu\bar{\nu}$ emission in free-bound and bound-bound transitions of partially ionized elements heavier than hydrogen and helium. These latter processes dominate in the energy range of a few keV and thus carry information about the solar metallicity. To calculate their rate we use libraries of monochromatic photon radiative opacities in analogy to a previous calculation of solar axion emission. Our overall flux spectrum and many details differ significantly from previous works. While this low-energy flux is not measurable with present-day technology, it could become a significant background for future direct searches for keV-mass sterile neutrino dark matter.

Contents

1	Introduction	1
2	Plasmon decay	4
2.1	Matrix element	4
2.2	Nonrelativistic limit	5
2.3	Decay rate and spectrum	6
2.4	Thermal emission spectrum	7
2.5	Compton pole process?	8
2.6	Solar neutrino flux	9
3	Photo production	11
3.1	Matrix element and decay rate	11
3.2	Correlation effects	12
3.3	Solar neutrino flux	14
4	Bremsstrahlung	15
4.1	Matrix element	15
4.2	Emission rate	16
4.3	Photon and axion emission	17
4.4	Medium response function and screening effects	18
4.5	Electron-electron bremsstrahlung	19
4.6	Solar neutrino flux	20
4.7	Beyond the Born approximation	21
5	Free-bound and bound-bound transitions	23
6	Solar neutrino flux at Earth	24
6.1	Flavor-dependent fluxes	24
6.2	Including flavor mixing	25
7	Discussion and summary	26
A	Standard solar model	27

1 Introduction

The nuclear reactions producing energy in the Sun also produce the well-known solar neutrino flux of about $6.6 \times 10^{10} \text{ cm}^{-2} \text{ s}^{-1}$ with MeV energies. At Earth this is the largest neutrino flux, except perhaps in the immediate vicinity of a nuclear power reactor. The role of solar neutrinos for the discovery of leptonic flavor conversion and for pioneering the field of astroparticle physics cannot be overstated. It is a remarkable shift of paradigm that solar neutrinos today, fifty years after their first detection, are part of the “neutrino floor,” the dominant background for direct searches of dark matter in the form of weakly interacting massive particles (WIMPs).

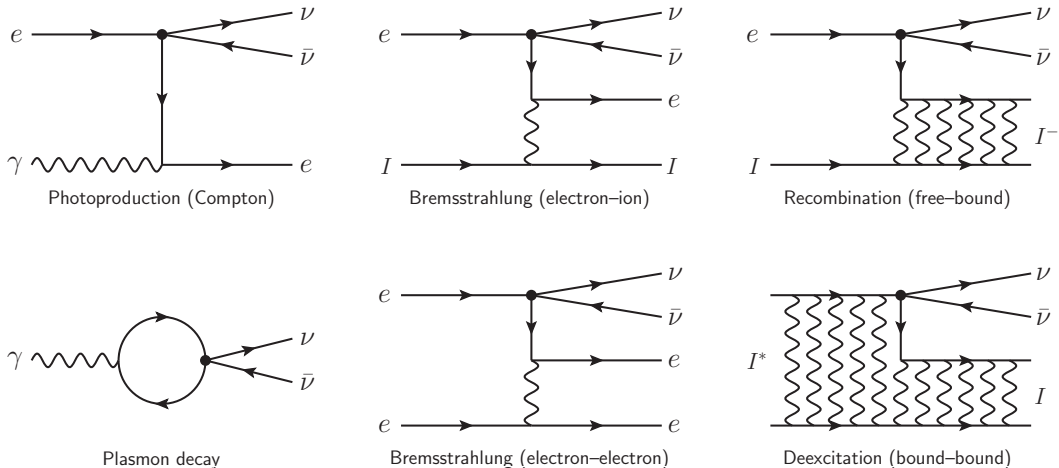


Figure 1. Processes for thermal neutrino pair production in the Sun.

Another well-motivated dark matter candidate is a sterile neutrino in the keV mass range [1]. One idea for a direct search is the sterile-neutrino capture on a stable isotope of dysprosium if $m_s > 2.83$ keV [2]. Other searches for slightly heavier sterile neutrinos include unstable isotopes [3, 4], coherent inelastic scattering on atoms [5] and electron scattering [6]. Once again, solar neutrinos could be a limiting background, now those with keV energies that emerge from various thermal processes in the solar plasma which has a typical temperature of 1 keV. While this idea is futuristic with present-day technology, it motivates us to consider keV-range solar neutrinos. This is a standard neutrino flux, yet it is conspicuously absent from a popular plot of the “grand unified neutrino spectrum” at Earth that ranges from cosmic background neutrinos to those from cosmic-ray sources at EeV energies [7].¹ The only detailed previous study of the keV range solar flux [8] ignores bremsstrahlung production and overestimates photo production by a spurious plasmon resonance. This situation motivates us to take a completely fresh look, taking advantage of recent progress in calculating the keV-range solar flux of other low-mass particles such as axions and hidden photons [9–14].

Thermal neutrino emission from stars is an old topic, central to the physics of stellar evolution, and detailed studies exist as well as Computer routines to be coupled with stellar evolution codes [15]. However, in this context neutrinos play the role of a local energy sink for the stellar plasma and so the emission spectrum is not provided. Moreover, for a low-mass main-sequence star like our Sun, energy loss by thermal neutrinos is negligible. Therefore, standard energy-loss rates, which cover a large range of temperatures, densities and chemical compositions, may not be optimized for solar conditions.

Low-energy neutrinos are produced in the solar plasma by the pair-production processes shown in figure 1, where nonrelativistic electrons are the sources. Electron velocities and spins are “kicked” by the ambient electromagnetic fields, leading to the emission of neutrino pairs. At low energies, the weak interaction is sufficiently well described by an effective four-fermion local interaction proportional to the Fermi constant G_F . The effective coupling constants for the vector and axial-vector interaction, C_V and C_A , are different for ν_e and the other flavors, leading to a nontrivial flavor dependence of the emitted fluxes. The vector-current interaction leads essentially to electric dipole radiation caused by the time variation

¹See also the IceCube MasterClass at <http://masterclass.icecube.wisc.edu/en/learn/detecting-neutrinos>.

of the electron velocity, whereas the axial-vector current leads to magnetic dipole radiation caused by fluctuations of the electron spin. Yet in the nonrelativistic limit, the rates for both mechanisms are related by simple numerical factors and there is no interference between them, so all processes provide rates proportional to $(a C_V^2 + b C_A^2) G_F^2$ with coefficients a and b that depend on the specific emission process. One consequence of this simple structure is that the emission rates are closely related to those for axions (axial current interaction) or hidden photons (vector current interaction) and also closely related to photon absorption rates. We will take full advantage of these similarities, i.e., the relation between these different processes by simple phase-space factors.

In figure 2 we show the overall low-energy solar neutrino and antineutrino flux at Earth from our calculation. All thermal processes shown in figure 1 produce $\nu\bar{\nu}$ pairs and thus equal fluxes of neutrinos and antineutrinos. This equipartition is another consequence of the nonrelativistic approximation, where weak magnetism effects disappear along with $C_V C_A$ cross terms in the emission rate [16]. In addition, the low-energy tail of the neutrino spectrum produced in the nuclear pp reaction contributes significantly to the keV flux. At the source,

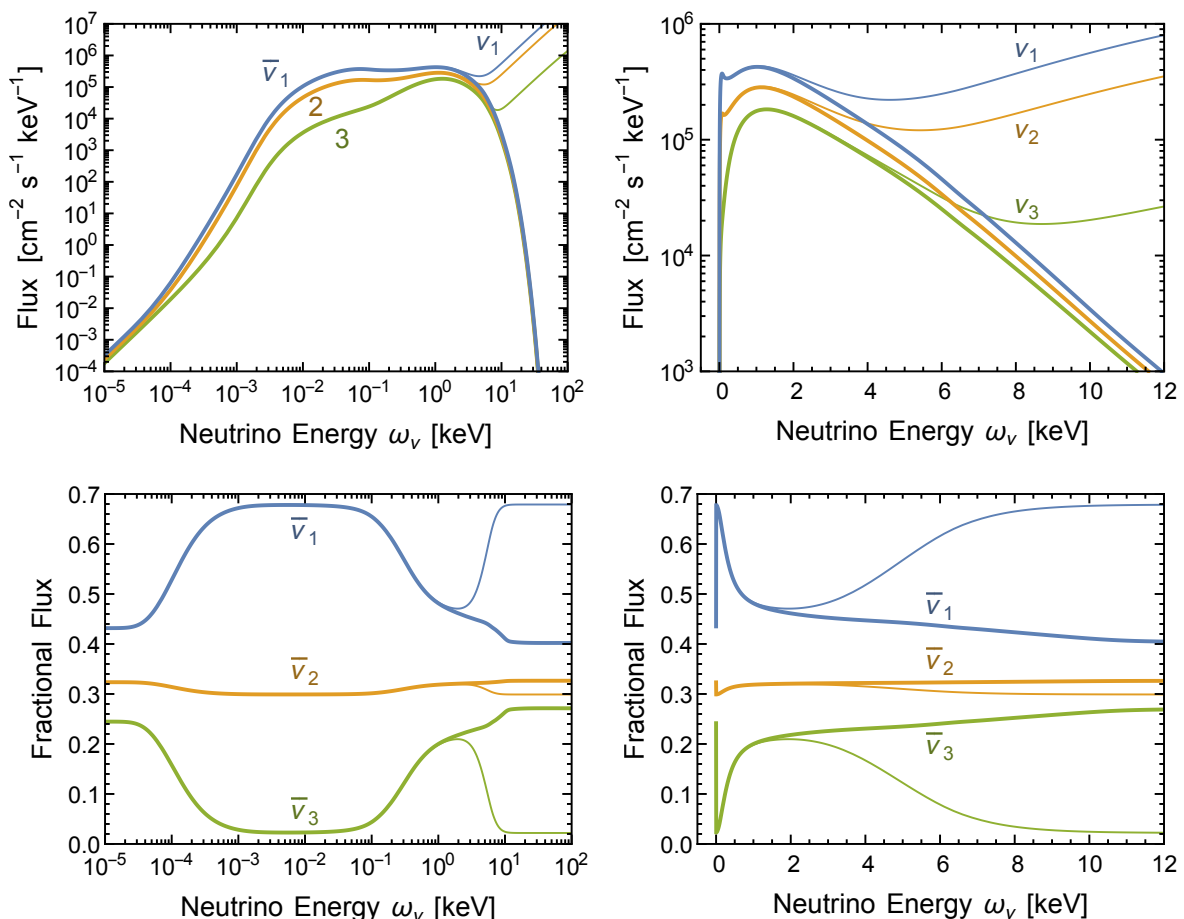


Figure 2. Solar neutrino flux at Earth in the keV range. The flavor dependence is given in the mass basis for the 1, 2 and 3 mass eigenstates (blue, orange and green). Thick lines are for $\bar{\nu}$, thin lines for ν which includes a contribution from the nuclear pp reaction which produces only ν_e at the source. The other source channels are thermal reactions which produce ν and $\bar{\nu}$ in equal measure. The bottom panels show the fractions of the total flux provided by the individual mass eigenstates.

this reaction produces ν_e which, like the other channels, have decohered into their mass components long before they reach Earth. The pp flux causes an overall asymmetry between the keV-range ν and $\bar{\nu}$ spectra. The fractional contribution of the 1, 2 and 3 mass eigenstates arriving at Earth are shown in the lower panels of figure 2. Different emission processes have different energy dependences and there are different coefficients ($a C_V^2 + b C_A^2$) for ν_e and the other flavors, thus explaining the fractional flux variation.

The rest of the paper is devoted to deriving the results shown in figure 2. In sections 2–5 we study individual processes. In section 6 we derive the overall flux at Earth after integration over a standard solar model which is detailed in appendix A. Section 7 is finally devoted to a summary and discussion.

2 Plasmon decay

2.1 Matrix element

We begin our calculation of neutrino pair emission from the solar interior with plasmon decay, $\gamma \rightarrow \nu\bar{\nu}$, the process of figure 1 involving the smallest number of participating particles. This process is also special in that it has no counterpart for axion emission. In any medium, electromagnetic excitations with wave vector $k = (\omega, \mathbf{k})$ acquire a nontrivial dispersion relation that can be written in the form $\omega^2 - \mathbf{k}^2 = \Pi(\mathbf{k})$, where $\Pi_{\mathbf{k}} = \Pi(\mathbf{k})$ is the on-shell polarization function. We will always consider an unmagnetized and isotropic plasma. It supports both transverse (T) modes, corresponding to the usual photons, and longitudinal (L) modes, corresponding to collective oscillations of electrons against ions. Whenever $\Pi_{\mathbf{k}} > 0$ (time like dispersion), the decay into a neutrino pair, taken to be massless, is kinematically allowed. For both T and L modes, neutrino pairs are actually emitted by electrons which oscillate coherently as a manifestation of the plasma wave.

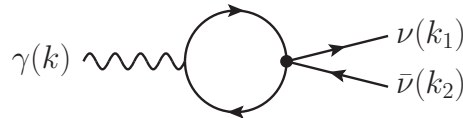


Figure 3. Plasmon decay mediated by electrons of the medium.

Therefore, plasmon decay and actually all other processes relevant for thermal pair emission in the Sun depend on the neutrino-electron interaction. At low energies, it is given by the effective neutral-current interaction

$$\mathcal{L}_{\text{int}} = \frac{G_{\text{F}}}{\sqrt{2}} \bar{\psi}_e \gamma^\mu (C_V - C_A \gamma_5) \psi_e \bar{\psi}_\nu \gamma_\mu (1 - \gamma_5) \psi_\nu, \quad (2.1)$$

where G_{F} is Fermi’s constant. The effective vector (V) and axial-vector (A) coupling constants include a neutral-current contribution and for ν_e also a charged-current piece from W^\pm exchange. Altogether one finds

$$C_V = \frac{1}{2}(4 \sin \Theta_{\text{W}} + 1) \quad \text{and} \quad C_A = +\frac{1}{2} \quad \text{for } \nu_e, \quad (2.2a)$$

$$C_V = \frac{1}{2}(4 \sin \Theta_{\text{W}} - 1) \quad \text{and} \quad C_A = -\frac{1}{2} \quad \text{for } \nu_\mu \text{ and } \nu_\tau, \quad (2.2b)$$

where $4 \sin^2 \Theta_{\text{W}} = 0.92488$ in terms of the weak mixing angle. In particular, this implies that the rates of A processes, proportional to $C_A^2 = 1/4$, are the same for all flavors. On the

other hand, the rates for V processes are proportional to

$$C_V^2 = 0.9263 \text{ for } \nu_e \bar{\nu}_e \quad \text{and} \quad C_V^2 = 0.0014 \text{ for } \nu_{\mu,\tau} \bar{\nu}_{\mu,\tau}. \quad (2.3)$$

Thus for heavy-lepton neutrinos we may safely ignore the vector-current interaction, i.e., such processes produce an almost pure $\nu_e \bar{\nu}_e$ flux.

Plasmon decay has been extensively studied in the literature [17–21]. The squared matrix element for the transition $\gamma \rightarrow \nu \bar{\nu}$ with photon four-momentum $k = (\omega, \mathbf{k})$ and ν and $\bar{\nu}$ four momenta $k_1 = (\omega_1, \mathbf{k}_1)$ and $k_2 = (\omega_2, \mathbf{k}_2)$ is found to be (see figure 3),

$$|\mathcal{M}_{\gamma \rightarrow \nu \bar{\nu}}|^2 = \frac{C_V^2 G_F^2}{8\pi\alpha} Z_{\mathbf{k}} \Pi_{\mathbf{k}}^2 \epsilon_{\mu} \epsilon_{\nu}^* N^{\mu\nu}, \quad (2.4)$$

where $\alpha = e^2/4\pi$ is the fine-structure constant. $Z_{\mathbf{k}}$ is the on-shell wave-function renormalization factor and $\Pi_{\mathbf{k}}$ the polarization factor appropriate for the T or L excitation. The photon polarization vector is ϵ^{μ} with $\epsilon^{\mu} \epsilon_{\mu}^* = -1$. The neutrino tensor, appearing in all pair emission processes, is

$$N^{\mu\nu} = 8(k_1^{\mu} k_2^{\nu} + k_1^{\nu} k_2^{\mu} - k_1 \cdot k_2 g^{\mu\nu} + i \varepsilon^{\alpha\mu\beta\nu} k_{1\alpha} k_{2\beta}). \quad (2.5)$$

Inserting this expression in the squared matrix element yields

$$|\mathcal{M}_{\gamma \rightarrow \nu \bar{\nu}}|^2 = \frac{C_V^2 G_F^2}{\pi\alpha} Z_{\mathbf{k}} \Pi_{\mathbf{k}}^2 (\epsilon^* \cdot k_1 \epsilon \cdot k_2 + \epsilon \cdot k_1 \epsilon^* \cdot k_2 + k_1 \cdot k_2). \quad (2.6)$$

Notice that the axial-vector interaction does not induce plasmon decay under the approximations described. This is particularly obvious in the nonrelativistic limit where we can think of the emission process as dipole radiation from coherently oscillating electrons, whereas the electron spins, responsible for non-relativistic axial-current processes, do not oscillate coherently. The absence of a sizeable axial-current rate implies that plasmon decay produces with high accuracy only $\nu_e \bar{\nu}_e$ pairs.

2.2 Nonrelativistic limit

In a classical plasma (nonrelativistic and nondegenerate), the electromagnetic dispersion relations for transverse (T) and longitudinal (L) plasmons are found to be

$$\omega^2|_{\text{T}} = \omega_{\text{p}}^2 \left(1 + \frac{\mathbf{k}^2}{\omega_{\text{p}}^2 + \mathbf{k}^2} \frac{T}{m_e} \right) + \mathbf{k}^2 \quad \text{and} \quad \omega^2|_{\text{L}} = \omega_{\text{p}}^2 \left(1 + 3 \frac{\mathbf{k}^2}{\omega_{\text{p}}^2} \frac{T}{m_e} \right). \quad (2.7)$$

The plasma frequency is given in terms of the electron density n_e by

$$\omega_{\text{p}}^2 = \frac{4\pi\alpha n_e}{m_e}. \quad (2.8)$$

In the Sun, $T \lesssim 1.3$ keV so that $T/m_e \lesssim 0.0025$ and with excellent approximation we may limit our discussion to the lowest-order term. Moreover, the lowest-order expression pertains to any level of degeneracy as long as the electrons remain nonrelativistic. In this case, T modes propagate in the same way as particles with mass ω_{p} , i.e., $\omega^2 = \mathbf{k}^2 + \omega_{\text{p}}^2$, whereas L modes oscillate with a fixed frequency $\omega = \omega_{\text{p}}$, independently of \mathbf{k} . Therefore, the L-plasmon dispersion relation is time-like only for $|\mathbf{k}| < \omega_{\text{p}}$, so only these soft quanta can decay into neutrino pairs.

In the nonrelativistic limit and using Lorentz gauge one finds $Z_{\text{T}} = 1$, $\Pi_{\text{T}} = \omega_{\text{p}}^2$, $Z_{\text{L}} = \omega_{\text{p}}^2/(\omega_{\text{p}}^2 - \mathbf{k}^2)$ and $\Pi_{\text{L}} = \omega_{\text{p}}^2 - \mathbf{k}^2$. Without loss of generality, we may assume the photon to move in the z direction. The T polarization vectors are in this case $\epsilon^{\mu} = (0, 1, 0, 0)$ and $\epsilon^{\mu} = (0, 0, 1, 0)$, respectively, whereas the L case with $|\mathbf{k}| < \omega_{\text{p}}$ has $\epsilon^{\mu} = (|\mathbf{k}|, 0, 0, \omega_{\text{p}})/(\omega_{\text{p}}^2 - \mathbf{k}^2)^{1/2}$. In Coulomb gauge one finds different expressions for the L quantities.

2.3 Decay rate and spectrum

Next we consider the decay rate of a transverse or longitudinal on-shell plasmon with wave vector \mathbf{k} and ask for its decay rate

$$\Gamma_{\gamma \rightarrow \nu \bar{\nu}} = \int \frac{d^3 \mathbf{k}_1}{(2\pi)^3} \frac{d^3 \mathbf{k}_2}{(2\pi)^3} \frac{|\mathcal{M}_{\gamma \rightarrow \nu \bar{\nu}}|^2}{2\omega 2\omega_1 2\omega_2} (2\pi)^4 \delta^4(k - k_1 - k_2). \quad (2.9)$$

In a nonrelativistic plasma one easily finds the usual result

$$\Gamma_{\text{T}} = \Gamma_{\text{p}} \frac{\omega_{\text{p}}}{\omega_{\mathbf{k}}} \quad \text{and} \quad \Gamma_{\text{L}} = \Gamma_{\text{p}} \frac{(\omega_{\text{p}}^2 - \mathbf{k}^2)^2}{\omega_{\text{p}}^4} \quad \text{with} \quad \Gamma_{\text{p}} = \frac{C_{\text{V}}^2 G_{\text{F}}^2 \omega_{\text{p}}^5}{48 \pi^2 \alpha}. \quad (2.10)$$

For T plasmons $\omega_{\mathbf{k}} = (\omega_{\text{p}}^2 + \mathbf{k}^2)^{1/2}$ with $0 \leq |\mathbf{k}| < \infty$, whereas for L plasmons the decay is allowed for $0 \leq |\mathbf{k}| < \omega_{\text{p}}$. The T case is reminiscent of a decaying particle with mass ω_{p} where the laboratory decay rate is time-dilated by the factor $\omega_{\text{p}}/\omega_{\mathbf{k}}$. In the limit $\mathbf{k} \rightarrow 0$ both rates are the same. Indeed, in the limit of vanishing wave number one cannot distinguish a transverse from a longitudinal excitation.

We are primarily interested in the neutrino energy spectrum. The symmetry of the squared matrix element under the exchange $k_1 \leftrightarrow k_2$ implies that it is enough to find the ν spectrum which is identical to the one for $\bar{\nu}$. Therefore, in equation (2.9) we integrate over $d^3 \mathbf{k}_2$ to remove the momentum delta function, and over $d\Omega_1$ to remove the one for energy conservation. Overall, with $\omega_{\nu} = \omega_1$ we write the result in the form

$$\frac{d\Gamma}{d\omega_{\nu}} = \Gamma g(\omega_{\nu}), \quad (2.11)$$

where $g(\omega_{\nu})$ is a normalized function. For T plasmons, averaged over the two polarization states, we find

$$g_{\text{T}}(\omega_{\nu}) = \frac{3}{4} \frac{\mathbf{k}^2 + (\omega_{\mathbf{k}} - 2\omega_{\nu})^2}{|\mathbf{k}|^3} \quad \text{for} \quad \frac{\omega_{\mathbf{k}} - |\mathbf{k}|}{2} < \omega_{\nu} < \frac{\omega_{\mathbf{k}} + |\mathbf{k}|}{2} \quad (2.12)$$

and zero otherwise. If the T plasmon were an unpolarized massive spin-1 particle, this would be a top-hat spectrum on the shown interval, corresponding to isotropic emission boosted to the laboratory frame. However, the T plasmon misses the third polarization state so that even unpolarized T plasmons do not show this behavior. For L plasmons we find

$$g_{\text{L}}(\omega_{\nu}) = \frac{3}{2} \frac{\mathbf{k}^2 - (\omega_{\text{p}} - 2\omega_{\nu})^2}{|\mathbf{k}|^3} \quad \text{for} \quad \frac{\omega_{\text{p}} - |\mathbf{k}|}{2} < \omega_{\nu} < \frac{\omega_{\text{p}} + |\mathbf{k}|}{2} \quad (2.13)$$

and zero otherwise, with the additional constraint $0 \leq |\mathbf{k}| < \omega_{\text{p}}$.

We show these distributions in figure 4. Assuming equal ω for both types of excitations and also equal \mathbf{k} , the distributions add to a top-hat spectrum of the form $\frac{2}{3} g_{\text{T}}(\omega_{\nu}) + \frac{1}{3} g_{\text{L}}(\omega_{\nu}) = 1/|\mathbf{k}|$ on the interval $(\omega - |\mathbf{k}|)/2 < \omega_{\nu} < (\omega + |\mathbf{k}|)/2$, i.e., this average resembles the decay spectrum of an unpolarized spin-1 particle. However, the dispersion relations are different for T and L plasmons so that, for equal \mathbf{k} , they have different ω and these distributions are not on the same ω_{ν} interval. The only exception is the $\mathbf{k} \rightarrow 0$ limit when $\omega \rightarrow \omega_{\text{p}}$ for both types.

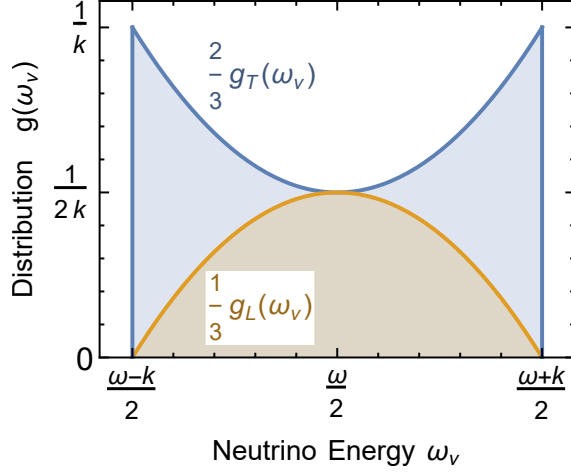


Figure 4. Normalized ν spectrum from transverse and longitudinal plasmon decay $\gamma \rightarrow \nu\bar{\nu}$. For T plasmons $\omega = (\omega_p^2 + \mathbf{k}^2)^{1/2}$, whereas for L plasmons $\omega = \omega_p$.

2.4 Thermal emission spectrum

As our final result we determine the spectral emission density from a nonrelativistic plasma with temperature T . The number of neutrinos emitted per unit volume per unit time per unit energy interval from T plasmon decay is

$$\frac{d\dot{n}_\nu}{d\omega_\nu}\Big|_T = \int_{V_{\mathbf{k}}} \frac{d^3\mathbf{k}}{(2\pi)^3} \frac{2\Gamma_T g_T(\omega_\nu)}{e^{\omega_{\mathbf{k}}/T} - 1} = \frac{3\Gamma_p \omega_p T}{4\pi^2} \int_{\omega_\nu + \frac{\omega_p^2}{4\omega_\nu}}^{\infty} \frac{d\omega}{T} \frac{1}{e^{\omega/T} - 1} \left[1 + \frac{(\omega - 2\omega_\nu)^2}{\omega^2 - \omega_p^2} \right]. \quad (2.14)$$

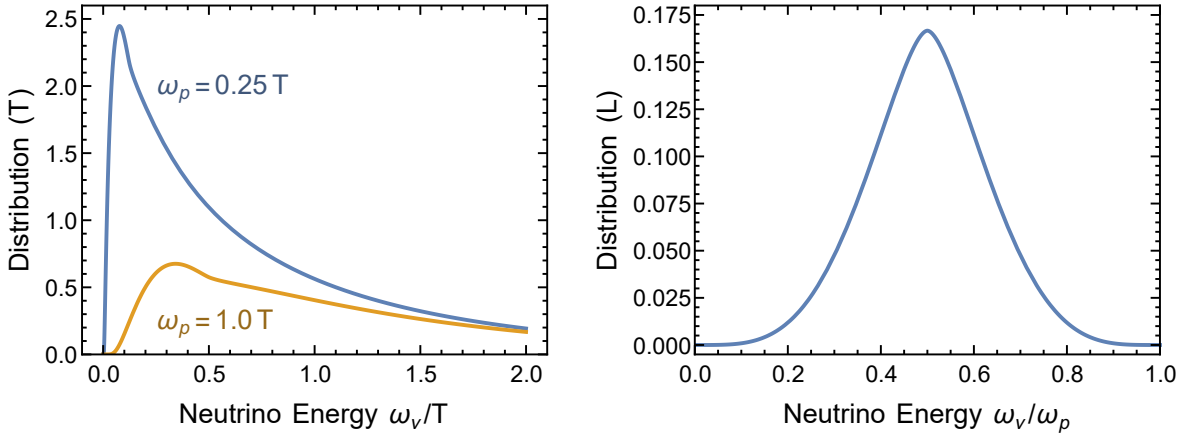


Figure 5. Neutrino spectrum from thermal plasmon decay. *Left panel:* Transverse plasmons. The curves represent the dimensionless integral in equation (2.14) and correspond to $\omega_p/T = 0.25$ and 1 as indicated. *Right panel:* Longitudinal plasmons. The curve is the dimensionless integral in equation (2.15). To make the vertical scale comparable to T plasmons, a factor $(\omega_p/T)/(e^{\omega_p/T} - 1) = 1 + \mathcal{O}(\omega_p/T)$ must be included.

The integration is over the volume in \mathbf{k} -space allowed by the decay kinematics given in equation (2.12) and the factor of 2 accounts for two transverse degrees of freedom. For $\omega_\nu \ll \omega_p$ the required plasmon energy is large so that we may approximate $e^{\omega/T} - 1 \rightarrow e^{\omega/T}$ and $(\omega - 2\omega_\nu)^2/(\omega^2 - \omega_p^2) \rightarrow 1$. In this case the dimensionless integral is $2e^{-\omega_p^2/4\omega_\nu T}$, i.e., this neutrino flux is exponentially suppressed at low energies due to the exponential suppression of the density of T-plasmons with sufficient energy. In figure 5 we show the dimensionless integral as a function of ω_ν/T for $\omega_p/T = 0.25$ and 1. Notice that in the central solar region $T = 1.3$ keV and $\omega_p = 0.3$ keV so that $\omega_p/T = 0.25$ corresponds approximately to conditions of the central Sun. The external shells of the Sun, where ω_p^2/T is smaller, turn out to be relevant for the lowest energy neutrinos from T-plasmon decay. However, we show later that this contribution is subdominant.

For L plasmons, the integral over the initial photon distribution yields the spectrum of the number emission rate

$$\begin{aligned} \left. \frac{d\dot{n}_\nu}{d\omega_\nu} \right|_L &= \int_{V_{\mathbf{k}}} \frac{d^3\mathbf{k}}{(2\pi)^3} \frac{\Gamma_L g_L(\omega_\nu)}{e^{\omega_p/T} - 1} \\ &= \frac{3\Gamma_p \omega_p^2}{4\pi^2 (e^{\omega_p/T} - 1)} \int_{|\omega_p - 2\omega_\nu|}^{\omega_p} d|\mathbf{k}| \frac{|\mathbf{k}| (\omega_p^2 - \mathbf{k}^2)^2}{\omega_p^6} \left[1 - \frac{(\omega_p - 2\omega_\nu)^2}{\mathbf{k}^2} \right] \\ &= \frac{3\Gamma_p \omega_p T}{4\pi^2} \frac{\omega_p/T}{e^{\omega_p/T} - 1} \left(\frac{2 + 3y^2 - 6y^4 + y^6}{12} + y^2 \log |y| \right), \end{aligned} \quad (2.15)$$

where $y = (2\omega_\nu - \omega_p)/\omega_p$ equivalent to $\omega_\nu = (y + 1)\omega_p/2$. L plasmons have the fixed energy ω_p , yet neutrinos from decay occupy the full interval $0 < \omega_\nu < \omega_p$ owing to the peculiar L dispersion relation. The neutrino distribution is symmetric relative to $\omega_\nu = \omega_p/2$. In figure 5 we show the dimensionless ω_ν distribution which is universal for any value of ω_p .

For $\omega_\nu \ll \omega_p$ the dimensionless integral can be expanded and yields $(32/3)(\omega_\nu/\omega_p)^4$, i.e., the spectrum decreases as a power law. Because the T-plasmon spectrum decreases exponentially, the L-plasmon decay provides the dominant neutrino flux at very low ω_ν . We illustrate this point in figure 6 where we show both spectra in common units of $3\Gamma_p \omega_p T/4\pi^2$ for $\omega_p/T = 0.25$ on a log-log-plot. The central solar temperature is 1.3 keV, so L-plasmon decay takes over for sub-eV neutrinos where the overall rate is extremely small.

2.5 Compton pole process?

Thus far we have used kinetic theory in that we treat the excitations of the medium as free particles which propagate until they decay or collide. Plasmons were treated as quasi-stable excitations, distributed as an ideal Bose gas, which occasionally decay into a neutrino pair. In a previous study of solar thermal neutrino emission [8] another channel was considered in the form $\gamma + e^- \rightarrow e^- + \gamma$ followed by $\gamma \rightarrow \nu\bar{\nu}$, i.e., the decaying plasmon was treated as an intermediate virtual particle in a Compton-like process. In its propagator, an imaginary part (a width) was included, but it was stressed that this width is small and that one needs to integrate over a narrow range of virtual energy-momenta near the on-shell condition. This ‘‘Compton plasmon pole’’ process was found to dominate thermal pair emission, a finding that would change everything about neutrino energy losses from stars.

However, we think this result is spurious. In a plasma, of course any particle is an intermediate state between collisions and as such a pole in a more complicated process. It

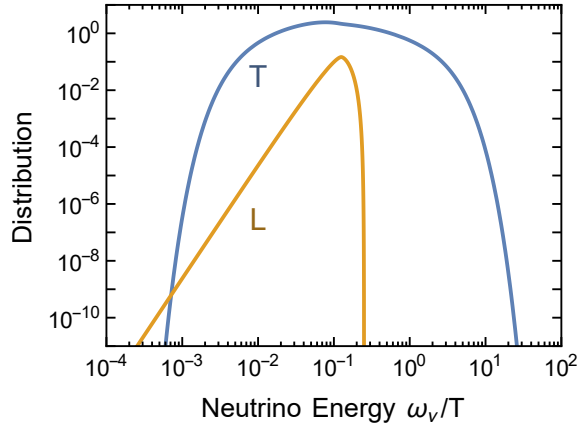


Figure 6. Neutrino spectrum from thermal T and L plasmon decay for $\omega_p/T = 0.25$ in units of $3\Gamma_p\omega_p T/4\pi^2$. At very low energies, L-plasmon decay dominates.

is the very basis of the kinetic approach to treat particles as on-shell states coming from far away without memory of their previous history. This assumption need not always be justified, but there is no particular reason why in the present context it should not apply to the plasmon. Its width is very small as stressed in reference [8].

On the other hand, it is not wrong to trace the plasmon one step back in its collision history. In this case one must be consistent, however, as to which processes produce and absorb plasmons and are thus responsible for its width. In reference [8] the plasmon width was taken as a complicated expression from the literature based essentially on inverse bremsstrahlung, whereas the last thing the plasmon did before decaying was taken to be Compton scattering. In this way, their equation (11) includes in the numerator essentially the Compton production rate, in the denominator the imaginary part of the propagator based on inverse bremsstrahlung. The emission rate gets spuriously enhanced by a large ratio of plasmon interaction rates based on different processes.

In summary, as long as the plasmon width is small, as everybody agrees it is, the “pole process” is identical with the plasmon decay process, not a new contribution. The only difference is that for a given momentum, the plasmon energy distribution is taken to follow a delta function (plasmon decay) or a narrow resonance distribution (pole process). The overall normalization is the same in both cases.

2.6 Solar neutrino flux

We finally integrate the plasmon decay rate over a standard solar model and show the expected neutrino flux at Earth in figure 7. We specifically use a solar model from the Saclay group which is described in more detail in appendix A. At this stage we do not worry about flavor oscillations and simply give the all-flavor flux at Earth, recalling that plasmon decay produces pure $\nu_e\bar{\nu}_e$ pairs at the source. We find

$$\Phi_T = 4.12 \times 10^5 \text{ cm}^{-2} \text{ s}^{-1} \quad \text{and} \quad \Phi_L = 4.67 \times 10^3 \text{ cm}^{-2} \text{ s}^{-1} \quad (2.16)$$

for the integrated fluxes at Earth.

The T plasmon flux now reaches much smaller energies than in figure 6 when we considered conditions near the solar center. Very low-energy neutrinos from plasmon decay require the plasmon to be very relativistic because the accessible energy range is $\omega - |\mathbf{k}| < \omega_\nu < \omega + |\mathbf{k}|$,

so the low energy flux is exponentially suppressed due to the exponential suppression of the density of high-energy plasmons. At larger solar radii T is smaller, but ω_p drops even faster and T plasmons are more relativistic. Therefore, lower-energy neutrinos become kinematically allowed, i.e., lower-energy neutrinos derive from larger solar radii. From figure 7 we conclude that the L plasmon flux begins to dominate at energies so low that the assumption of massless neutrinos is not necessarily justified.

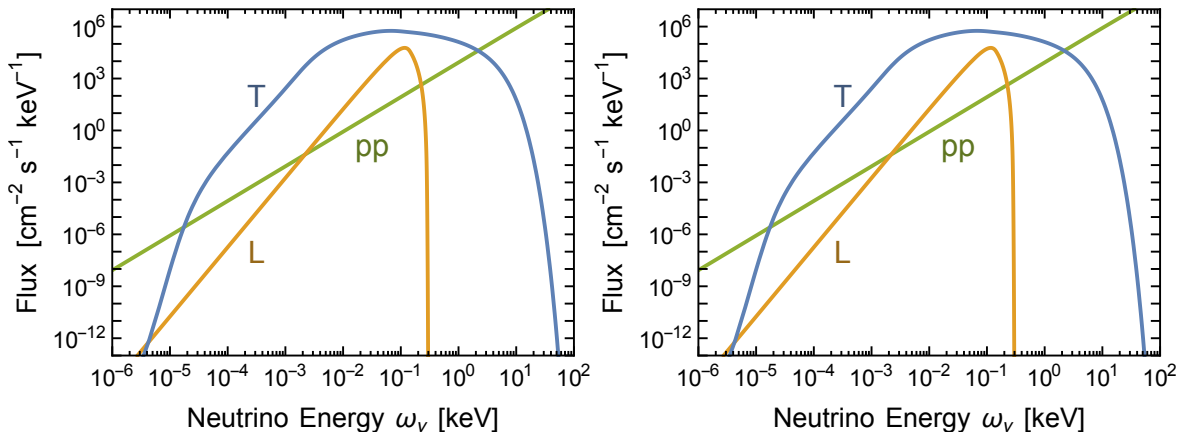


Figure 7. Solar neutrino flux at Earth from transverse and longitudinal plasmon decay. This is the total ν flux produced as nearly pure ν_e in the Sun. There is an equal $\bar{\nu}$ flux. We also show the low-energy tail of the usual flux from the nuclear pp reaction which are born as ν_e .

For comparison we also show the ν flux from the pp reaction that produces the lowest-energy flux from nuclear reactions. All standard solar models agree on this flux within around 1%, so we may use as a generic number $6.0 \times 10^{10} \text{ cm}^{-2} \text{ s}^{-1}$. The reaction $p + p \rightarrow d + e^+ + \nu_e$ has a neutrino endpoint energy of $Q = 420.22 \text{ keV}$. Including the thermal kinetic energy of the protons in the solar plasma, the overall endpoint of the solar spectrum is $Q = 423.41 \text{ keV}$ [22]. This reference also gives a numerical tabulation of the solar ν_e spectrum from the pp reaction. Ignoring a small e^+ final-state correction, the spectrum follows that of an allowed weak transition of the normalized form

$$\begin{aligned} \frac{dN}{d\omega_\nu} &= \frac{\omega_\nu^2 (Q + m_e - \omega_\nu) \sqrt{(Q + m_e - \omega_\nu)^2 - m_e^2}}{A^5} \\ &= \frac{(Q + m_e) \sqrt{Q(Q + 2m_e)}}{A^5} \omega_\nu^2 + \mathcal{O}(\omega_\nu^3) \end{aligned} \quad (2.17)$$

where $A = 350.8 \text{ keV}$ if we use the solar endpoint energy. The analytic form of the normalization factor A is too complicated to be shown here. The low-energy pp flux spectrum at Earth is the power law

$$\frac{d\Phi_{pp}}{d\omega_\nu} = 8150 \text{ cm}^{-2} \text{ s}^{-1} \text{ keV}^{-1} \left(\frac{\omega_\nu}{\text{keV}} \right)^2, \quad (2.18)$$

an approximation that is good to about $\pm 1.5\%$ for energies below 10 keV. This shallow power law is simply determined by the low-energy neutrino phase space. It dominates over plasmon decay at very low energies, although, of course, it does not produce antineutrinos. We will show later that both are subdominant compared to the neutrino flux produced in bremsstrahlung transitions.

3 Photo production

3.1 Matrix element and decay rate

The Compton process (figure 8), also known as photo production or photoneutrino production, was one of the first processes to be considered as an energy-loss mechanism for stars [23–25]. In these older papers, only the energy-loss rate was calculated, whereas the neutrino spectrum was calculated in the nonrelativistic limit in reference [8] and for general kinematics in reference [26]. We restrict ourselves to the nonrelativistic limit where electron recoils are neglected. The process then amounts to the conversion $\gamma \rightarrow \nu\bar{\nu}$, catalyzed through bystander electrons which take up three-momentum, and as such is somewhat similar to plasmon decay. However, no plasma mass is needed because momentum is taken up by the electrons. Even though we neglect recoils, the process is not “forward” for the electrons. We can interpret plasmon decay as the coherent version of photo production.

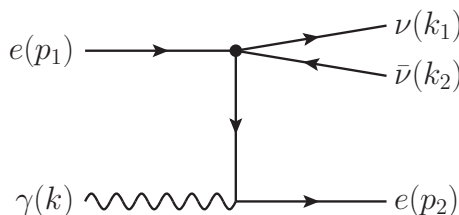


Figure 8. Photo production of neutrino pairs (Compton process). A second diagram with vertices interchanged is not shown.

In the nonrelativistic limit we find for the squared matrix element, averaged over initial spins and polarizations and summed over final ones,

$$\overline{|\mathcal{M}|^2} = \frac{1}{4} \sum_{\epsilon, s_1, s_2} |\mathcal{M}|^2 = \frac{e^2 G_F^2}{\omega^2} M^{\mu\nu} N_{\mu\nu} \quad (3.1)$$

where the neutrino tensor was given in equation (2.5). The nonrelativistic electron tensor for the Compton process is [8]

$$M^{\mu\nu} = \sum_{\epsilon} \left\{ (C_V^2 + C_A^2) (-\omega\epsilon^\mu + \delta^{\mu 0}\epsilon \cdot q) (-\omega\epsilon^\nu + \delta^{\nu 0}\epsilon \cdot q) + C_A^2 [k^\mu k^\nu - (\epsilon \cdot q)^2 g^{\mu\nu}] \right\}, \quad (3.2)$$

where ϵ is the photon polarization vector and $q = k_1 + k_2$ the four momentum carried away by the neutrino pair.

It is noteworthy that both the vector and axial-vector currents contribute on comparable levels, in contrast to plasmon decay. This is heuristically understood if we observe that the vector part amounts to electric dipole emission by the electron being “shaken” by the incoming EM wave. The rate is proportional to $(G_F/m_e)^2$ because the outgoing radiation couples with strength G_F and the mass appears due to its inertia against the acceleration. Axial-current emission amounts to magnetic dipole emission caused by the electron spin. The coupling is through the electron dipole moment $\propto 1/m_e$, so the rate is also proportional to $(G_F/m_e)^2$. In the case of axion emission, $\gamma + e \rightarrow e + a$, enabled by a derivative axial-vector coupling, the rate is suppressed by a factor $(\omega/m_e)^2$ relative to Compton scattering. For neutrinos the coupling structure is the same for both axial and vector coupling. Note however

that these considerations require some handwaving and one should always check which terms in the nonrelativistic expansion of the Hamiltonian contribute to a certain order.

We use the symmetry under the exchange $1 \leftrightarrow 2$ and integrate over the phase space of $\bar{\nu}$ and over the angles of ν . With $\omega_p = 0$ we find for the differential “decay rate” of T plasmons with energy ω of either polarization

$$\frac{d\Gamma_\omega}{d\omega_\nu} = n_e \frac{2}{3} \frac{G_F^2 \alpha}{\pi^2 m_e^2} (C_V^2 + 5C_A^2) \frac{(\omega - \omega_\nu)^2 \omega_\nu^2}{\omega} \left[1 - \frac{2}{3} \frac{(\omega - \omega_\nu) \omega_\nu}{\omega^2} \right] \quad \text{for } \omega_\nu < \omega. \quad (3.3)$$

Integrated over the photon distribution it gives the familiar result [8]

$$\begin{aligned} \frac{d\dot{n}_\nu}{d\omega_\nu} &= n_e \frac{2}{3} \frac{G_F^2 \alpha}{\pi^4 m_e^2} \int_{\omega_\nu}^{\infty} d\omega \omega_\nu^2 (\omega - \omega_\nu)^2 \frac{1}{e^{\omega/T} - 1} \\ &\quad \times (C_V^2 + 5C_A^2) \omega \left[1 - \frac{2}{3} \frac{(\omega - \omega_\nu) \omega_\nu}{\omega^2} \right]. \end{aligned} \quad (3.4)$$

Including the modified dispersion relation in the plasma with a nonvanishing ω_p leads to a more complicated expression that modifies the result for ω near ω_p and by up to a few percent elsewhere, for us a negligible correction. On the other hand, at energies near ω_p , Compton emission is subdominant relative to plasmon decay. Moreover, one should then also worry about longitudinal plasmons which can be understood as collective electron oscillations. One therefore would need to avoid double counting between $\gamma_L + e \rightarrow e + \nu\bar{\nu}$ and bremsstrahlung $e + e \rightarrow e + e + \nu\bar{\nu}$, see the related discussion in reference [34]. Therefore, we use the emission rate based on the $\omega_p = 0$ expression of equation (3.4), but we will include ω_p in the phase space of initial T plasmons, cutting off $\omega < \omega_p$ initial-state photons.

3.2 Correlation effects

So far we have assumed that electrons are completely uncorrelated and the overall neutrino emission rate is the incoherent sum from individual scattering events. However, electrons are anticorrelated by the Pauli exclusion principle and by Coulomb repulsion, both effects meaning that at the location of a given electron it is less likely than average to find another one. These anticorrelations lead to a reduction of the rate, i.e., we need to include a structure factor $S(\mathbf{q}^2)$ where $\mathbf{q} = \mathbf{k} - \mathbf{k}_1 - \mathbf{k}_2$ is the three-momentum transfer. For photon transport, exchange effects produce a 7% correction in the solar center and less elsewhere, whereas Coulomb correlations provide a 20–30% correction [27].

Beginning with the exchange correlation, a simple approach is to include a Pauli blocking factor $(1 - f_{\mathbf{p}})$ for the final state electron in the phase-space integration. For nonrelativistic electron targets that barely recoil, the final-state \mathbf{p} can be taken the same as the initial one, so the overall reduction is the average Pauli blocking factor

$$R_\eta = \frac{2}{n_e} \int \frac{d^3\mathbf{p}}{(2\pi)^3} f_{\mathbf{p}} (1 - f_{\mathbf{p}}) = \int_0^\infty \frac{dx x^2}{e^{x^2 - \eta} + 1} \left(1 - \frac{1}{e^{x^2 - \eta} + 1} \right) \bigg/ \int_0^\infty \frac{dx x^2}{e^{x^2 - \eta} + 1}, \quad (3.5)$$

where the nonrelativistic degeneracy parameter $\eta = (\mu - m_e)/T$ is given by

$$n_e = 2 \int \frac{d^3\mathbf{p}}{(2\pi)^3} \frac{1}{e^{\frac{\mathbf{p}^2}{2m_e T} - \eta} + 1}. \quad (3.6)$$

We have checked that this expression is indeed the $|\mathbf{q}| = \kappa \rightarrow 0$ limit of $1 + h_x(\kappa)$ given in equation (6) of reference [27]. In this paper and the literature on solar opacities, the Pauli blocking effect is interpreted as an anticorrelation of the electrons in analogy to what is caused by a repulsive force. So we can picture Pauli effects either as a blocking of final electron states in collisions or as an anticorrelation of initial-state electron targets.

Next we turn to Coulomb repulsion where for solar conditions the structure function can be reasonably approximated essentially by a Debye-Hückel screening prescription [27]

$$S_e(\mathbf{q}^2) = 1 - \frac{k_e^2}{\mathbf{q}^2 + k_e^2 + k_i^2}. \quad (3.7)$$

The screening scales are

$$k_e^2 = R_\eta \frac{4\pi\alpha n_e}{T} \quad \text{and} \quad k_i^2 = \frac{4\pi\alpha}{T} \sum_Z Z^2 n_Z, \quad (3.8)$$

where n_Z is the number density of ions with charge Ze . For electrons, we have included the correction factor R_η for partial degeneracy.² For conditions of the central Sun we have an electron density of about $n_e = 6.3 \times 10^{25} \text{ cm}^{-3}$ and a temperature $T = 1.3 \text{ keV}$, providing $\eta = -1.425$, leading to $R_\eta = 0.927$. The Debye-Hückel scales are $k_e = 5.4 \text{ keV}$ and $k_i = 7.0 \text{ keV}$. As these scales are comparable to a typical momentum transfer there is no simple limit for Coulomb corrections. In our numerical estimate of the solar emission we use a simple prescription to account for this effect: the largest possible momentum transfer for an initial photon of energy ω is $|\mathbf{q}_{\text{max}}| = 2\omega$. Using $S_e(4\omega^2)$ to multiply equation (3.3) provides an upper limit to the suppression caused by Coulomb correlations, i.e., the neutrino flux will be slightly overestimated.

Coulomb correlations apply to processes where the electron density is the crucial quantity, i.e., to the vector-current part proportional to C_V^2 . The axial-current contributions, proportional to C_A^2 , depend on the electron spins which are not correlated by Coulomb interactions. If an electron at a given location has a certain spin, the chance of finding one with the same or opposite spin at some distance is the same, i.e., the spins are not correlated. Therefore, the interference of spin-dependent scattering amplitudes from different electrons average to zero and we do not need any Coulomb correlation correction. Only the emission of $\nu_e \bar{\nu}_e$ has any V contribution and in all cases, the A term strongly dominates. Therefore, overall Coulomb corrections are small for photo production.

Treating exchange corrections as an average final-state Pauli blocking factor reveals that it applies for both V and A processes. We can also see this point in terms of initial-state correlations. Electrons of opposite spin are not correlated because they can occupy the same location, whereas those with equal spin “repel” each other. Therefore, the interference effects between initial electrons of equal and opposite spins do not average to zero.

In summary, the photo production rate is reduced by the overall Pauli blocking factor R_η given in equation (3.5) which in the Sun is a few percent. The terms proportional to C_V^2 , on the other hand, require the additional Coulomb structure factor given in equation (3.7) which can be a 30% correction. The V channel essentially applies only to $\nu_e \bar{\nu}_e$ emission, where Coulomb correlations provide an overall reduction of perhaps 10%.

²Our R_η defined in equation (3.5) is the same as R_α defined in reference [27] by a ratio of Fermi integrals. The overall structure factor was written in the form $1 + h_x(\kappa) + h_r(\kappa)$ with $h_r(\kappa) = -R_\eta k_e^2 / (\kappa^2 + k_e^2 + k_i^2)$. However, for the exchange correlations, the $\kappa \rightarrow 0$ limit is justified and $R_\eta = 1 + h_x(0)$ so that $1 + h_x + h_r = R_\eta - R_\eta k_e^2 / (\kappa^2 + k_e^2 + k_i^2) = R_\eta S_e(\kappa)$. In other words, the exchange correlations indeed amount to a global factor R_η for final-state Pauli blocking besides a reduction of the electron screening scale k_e^2 .

3.3 Solar neutrino flux

We now integrate the source reaction rate over our solar model and show the neutrino flux in figure 9 on a linear scale. The blue curve derives from the V channel and includes Coulomb correlations, whereas the orange curve applies to the A channel. To obtain the proper flux the curves need to be multiplied with C_V^2 and $5C_A^2$, respectively.

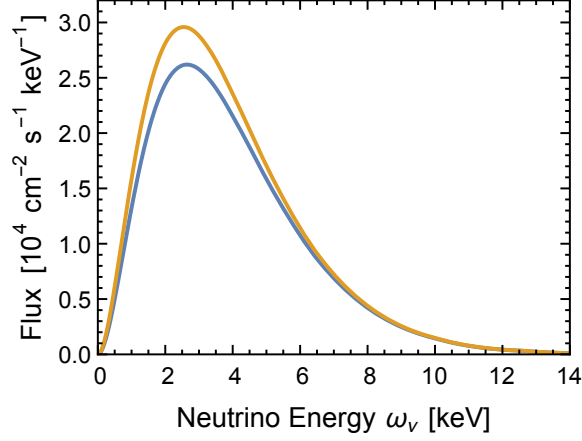


Figure 9. Neutrino flux from Compton production for the vector (blue) and axial-vector (orange) interaction. For the proper flux, the V curve is to be multiplied with C_V^2 , the A curve with $5C_A^2$. The difference between the blue and orange curves derives from Coulomb correlations which apply only to the V channel. The Coulomb correlations were treated in an approximate way as described in the text and the suppression could be slightly larger.

In figure 10 we compare the axial-vector Compton flux for a single flavor with the fluxes from T-plasmon decay and with pp neutrinos. While we have not included the plasma frequency in the squared matrix element for the Compton process, we do include it in the phase-space integration. In this way, the lowest-energy Compton flux is suppressed and explains the kink in the low-energy flux. As a consequence, the lowest-energy neutrino flux is dominated by plasmon decay. Notice that T-plasmon decay produces almost exclusively

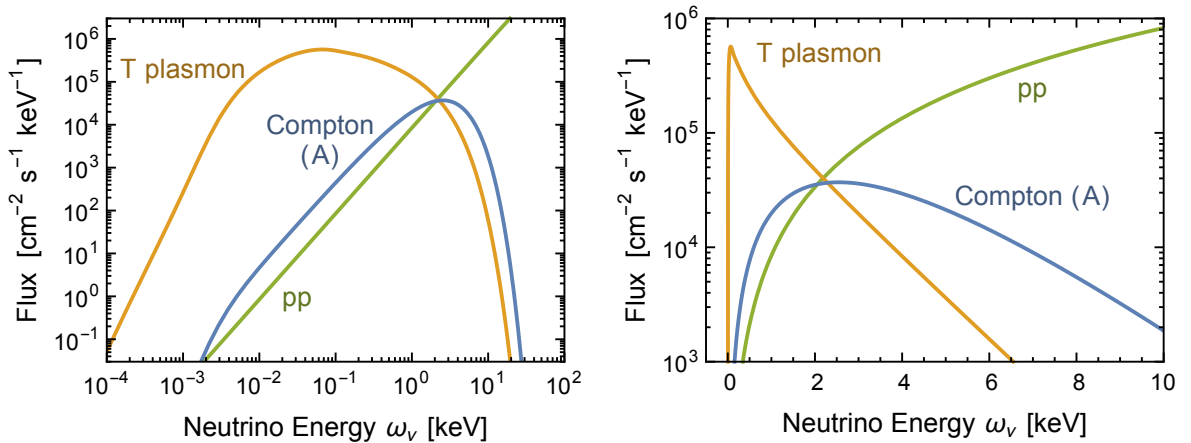


Figure 10. Solar neutrino flux at Earth from the Compton process (axial-vector channel and only one flavor) compared with the pp flux (only ν_e) and transverse plasmon decay (ν_e and equal flux $\bar{\nu}_e$). Flavor oscillations are not considered here.

$\nu_e \bar{\nu}_e$ pairs, whereas the axial-vector Compton process produces equal fluxes of all flavors. For $\nu_e \bar{\nu}_e$, there is an additional contribution from the V channel. Apart from Coulomb-correlation corrections and overall coefficients, the spectrum is the same as shown in figure 9. The flavor dependence of fluxes at Earth will be studied later.

4 Bremsstrahlung

4.1 Matrix element

Next we consider bremsstrahlung production of neutrino pairs (figure 11), also known as the free-free process, where we consider nuclei or ions with charge Ze to provide a Coulomb potential without recoil. This process was not included in a previous study of low-energy solar neutrino emission [8]. In general, it is the dominant energy loss mechanism in stars with low temperature and high electron density [28, 29]. The first differential flux evaluation was carried out for our nonrelativistic and nondegenerate conditions a long time ago in reference [30], which has some flaws as described below, and recently also for general conditions [31].

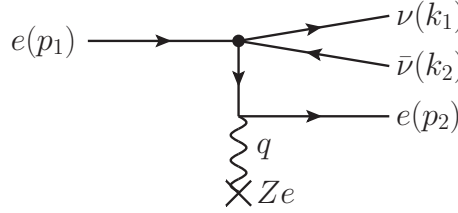


Figure 11. Bremsstrahlung production of neutrino pairs. The Coulomb potential is provided by a heavy nucleus or ion with charge Ze taking up the momentum transfer $q = (0, \mathbf{q})$. The outgoing neutrino radiation carries the four-momentum $k = k_1 + k_2 = (\omega, \mathbf{k})$. There is a second diagram with the vertices exchanged.

The scattering targets are taken to be very heavy (no recoil) with charge Ze and number density n_Z and the electrons are taken to be nonrelativistic. The emission rate of neutrino pairs per unit volume and unit time is then

$$\dot{n}_\nu = n_Z \int \frac{d^3 \mathbf{p}_1}{(2\pi)^3} \frac{d^3 \mathbf{p}_2}{(2\pi)^3} \frac{d^3 \mathbf{k}_1}{(2\pi)^3} \frac{d^3 \mathbf{k}_2}{(2\pi)^3} f_1 (1 - f_2) \frac{\sum_{s_1, s_2} |\mathcal{M}|^2}{(2m_e)^2 2\omega_1 2\omega_2} 2\pi \delta(E_1 - E_2 - \omega), \quad (4.1)$$

where the sum is taken over the electron spins and f_1 and f_2 are the initial and final-state electron occupation numbers. The final-state neutrino radiation is described by $k = (\omega, \mathbf{k}) = k_1 + k_2 = (\omega_1 + \omega_2, \mathbf{k}_1 + \mathbf{k}_2)$. For the squared matrix element we find

$$\sum_{s_1, s_2} |\mathcal{M}|^2 = \frac{8Z^2 e^4}{|\mathbf{q}|^4 \omega^2} \left(\frac{G_F^2}{2} \right) \left(C_V^2 M_V^{\mu\nu} + C_A^2 M_A^{\mu\nu} \right) N_{\mu\nu}, \quad (4.2)$$

where the neutrino tensor was given in equation (2.5) and \mathbf{q} is the momentum transfer to the nucleus.

For nonrelativistic electrons, as usual we can ignore the transfer of three-momentum to the external radiation so that $\mathbf{q} = \mathbf{p}_1 - \mathbf{p}_2$. In this approximation we find

$$M_V^{\mu\nu} = \begin{pmatrix} \left(\frac{\mathbf{q} \cdot \mathbf{k}}{\omega} \right)^2 & \frac{\mathbf{q} \cdot \mathbf{k}}{\omega} \mathbf{q} \\ \frac{\mathbf{q} \cdot \mathbf{k}}{\omega} \mathbf{q} & \mathbf{q}^i \mathbf{q}^j \end{pmatrix} \quad \text{and} \quad M_A^{\mu\nu} = \begin{pmatrix} \mathbf{q}^2 & \frac{\mathbf{q} \cdot \mathbf{k}}{\omega} \mathbf{q} \\ \frac{\mathbf{q} \cdot \mathbf{k}}{\omega} \mathbf{q} & \left(\frac{\mathbf{q} \cdot \mathbf{k}}{\omega} \right)^2 \delta^{ij} \end{pmatrix}. \quad (4.3)$$

With $C_V = C_A = 1$ one should find the bremsstrahlung rates in the old literature before the discovery of neutral currents. However, the terms proportional to $\mathbf{q}\cdot\mathbf{k}/\omega$ are missing (see the steps from equation 5 to 6 in reference [30]). For the V-case, bremsstrahlung arises from the electron velocity abruptly changing in a collision. In the nonrelativistic limit, the 0-component of the electron current remains unchanged. However, the squared matrix element is quadratic in the velocity change. Therefore, a consistent nonrelativistic expansion requires to go to second order in the small velocity everywhere. If one expands the electron current only to linear order before taking the matrix element one misses some of the terms. A similar issue explains the factor 2/3 difference in the axion bremsstrahlung calculation between reference [32] (equations 38 to 42) and [33] (equations 1 to 4).

The electron gas is assumed to be isotropic, so in equation (4.1) we may first perform an angle average over the electron direction, keeping their relative angle fixed. So we average over the relative angle between \mathbf{q} and \mathbf{k} , leading to $\mathbf{q}^i\mathbf{q}^j \rightarrow \frac{1}{3}\mathbf{q}^2\delta^{ij}$, $(\mathbf{q}\cdot\mathbf{k})\mathbf{q} \rightarrow \frac{1}{3}\mathbf{q}^2\mathbf{k}$, and $(\mathbf{q}\cdot\mathbf{k})^2 \rightarrow \frac{1}{3}\mathbf{q}^2\mathbf{k}^2$. Therefore, in an isotropic medium we may write

$$\left\langle \sum_{s_1, s_2} |\mathcal{M}|^2 \right\rangle_{\cos(\mathbf{q}, \mathbf{k})} = \frac{8Z^2 e^4}{3\mathbf{q}^2} \left(\frac{G_F^2}{2} \right) \frac{(C_V^2 \bar{M}_V^{\mu\nu} + C_A^2 \bar{M}_A^{\mu\nu}) N_{\mu\nu}}{\omega^4}, \quad (4.4)$$

where

$$\bar{M}_V^{\mu\nu} = \begin{pmatrix} \mathbf{k}^2 & \omega\mathbf{k} \\ \omega\mathbf{k} & \omega^2\delta^{ij} \end{pmatrix} \quad \text{and} \quad \bar{M}_A^{\mu\nu} = \begin{pmatrix} 3\omega^2 & \omega\mathbf{k} \\ \omega\mathbf{k} & \mathbf{k}^2\delta^{ij} \end{pmatrix}. \quad (4.5)$$

Notice that lowering the indices in this matrix changes the sign of the time-space part (the 0j and j0 components), i.e., lowering the indices amounts to $\omega\mathbf{k} \rightarrow -\omega\mathbf{k}$. For the contractions we find explicitly

$$\begin{aligned} \bar{M}_V^{\mu\nu} N_{\mu\nu} &= 16 [\omega_1\omega_2(\omega_1^2 + \omega_2^2 + \omega_1\omega_2) + (\mathbf{k}_1\cdot\mathbf{k}_2)^2 - \omega^2 \mathbf{k}_1\cdot\mathbf{k}_2] \\ &\rightarrow \frac{16}{3} \omega_1\omega_2 (3\omega_1^2 + 3\omega_2^2 + 4\omega_1\omega_2), \end{aligned} \quad (4.6a)$$

$$\begin{aligned} \bar{M}_A^{\mu\nu} N_{\mu\nu} &= 16 [\omega_1\omega_2(2\omega_1^2 + 2\omega_2^2 + \omega_1\omega_2) - (\mathbf{k}_1\cdot\mathbf{k}_2)^2 + 4\omega_1\omega_2 \mathbf{k}_1\cdot\mathbf{k}_2] \\ &\rightarrow \frac{32}{3} \omega_1\omega_2 (3\omega_1^2 + 3\omega_2^2 + \omega_1\omega_2). \end{aligned} \quad (4.6b)$$

The second expressions apply after an angle average over the relative directions of \mathbf{k}_1 and \mathbf{k}_2 where $\mathbf{k}_1\cdot\mathbf{k}_2 \rightarrow 0$ and $(\mathbf{k}_1\cdot\mathbf{k}_2)^2 \rightarrow \frac{1}{3}\omega_1^2\omega_2^2$.

4.2 Emission rate

We may write the neutrino pair emission rate of equation (4.1) in a way that separates the properties of the emitted radiation (the neutrino pairs) from the properties of the medium (thermal electrons interacting with nuclei) and find

$$\dot{n}_\nu = n_Z n_e \frac{8Z^2 \alpha^2}{3} \int \frac{d^3\mathbf{k}_1}{2\omega_1(2\pi)^3} \frac{d^3\mathbf{k}_2}{2\omega_2(2\pi)^3} \left(\frac{G_F}{\sqrt{2}} \right)^2 \frac{(C_V^2 \bar{M}_V^{\mu\nu} + C_A^2 \bar{M}_A^{\mu\nu}) N_{\mu\nu}}{\omega^4} \mathcal{S}(\omega), \quad (4.7)$$

where $\omega = \omega_1 + \omega_2$ is the energy carried away by a neutrino pair. Collecting coefficients in a slightly arbitrary way, the relevant response function of the medium is

$$\mathcal{S}(\omega) = \frac{(4\pi)^2}{(2m_e)^2} \frac{1}{n_e} \int \frac{d^3\mathbf{p}_1}{(2\pi)^3} \frac{d^3\mathbf{p}_2}{(2\pi)^3} f_1(1-f_2) \frac{1}{\mathbf{q}^2} 2\pi\delta(E_1 - E_2 - \omega), \quad (4.8)$$

where $\mathbf{q} = \mathbf{p}_1 - \mathbf{p}_2$ is the momentum transfer in the electron-nucleus collision mediated by the Coulomb field. We see that for both vector and axial vector emission it is the same property of the medium causing the emission. We will return to this point later for the free-bound and bound-bound emission processes because we can relate both vector and axial-vector processes to the monochromatic photon opacities, the latter providing us essentially with $\mathcal{S}(\omega)$.

We now integrate over neutrino emission angles and find the neutrino emission spectrum by using $\omega_1 = \omega_\nu$ and $\omega_2 = \omega - \omega_\nu$. Integrating over the anti-neutrino energy we find

$$\begin{aligned} \frac{d\dot{n}_\nu}{d\omega_\nu} = n_Z n_e \frac{8 Z^2 \alpha^2}{3} \left(\frac{G_F}{\sqrt{2}} \right)^2 \frac{1}{3\pi^4} \int_{\omega_\nu}^{\infty} d\omega \mathcal{S}(\omega) \frac{\omega_\nu^2 (\omega - \omega_\nu)^2}{\omega^4} \\ \times \left[C_V^2 (3\omega^2 - 2\omega\omega_\nu + 2\omega_\nu^2) + 2C_A^2 (3\omega^2 - 5\omega\omega_\nu + 5\omega_\nu^2) \right], \end{aligned} \quad (4.9)$$

which is the rate of neutrino emission per unit volume, unit time, and unit energy interval. The same spectrum applies to antineutrinos because all expressions were symmetric under the exchange $1 \leftrightarrow 2$.

4.3 Photon and axion emission

It is useful to compare the bremsstrahlung emission rate of neutrino pairs with that of photons and axions to connect to the previous literature and, more importantly, to relate the bremsstrahlung absorption rate of photons to the neutrino pair emission rate. For photon emission, the neutral-current interaction of equation (2.1) gets replaced by $ie\bar{\psi}_e\gamma^\mu\psi_e A_\mu$. On the level of the squared matrix element, or rather, on the level of the emission rate, this substitution translates to

$$\dot{n}_\gamma = n_Z n_e \frac{8 Z^2 \alpha^2}{3} \int \frac{d^3\mathbf{k}}{2\omega(2\pi)^3} e^2 \frac{\bar{M}_V^{\mu\nu} \epsilon_\mu \epsilon_\nu}{\omega^4} \mathcal{S}(\omega). \quad (4.10)$$

For the contraction we find $\bar{M}_V^{\mu\nu} \epsilon_\mu \epsilon_\nu = \omega^2$. We have used the polarization vector for a transverse photon (not a longitudinal plasmon) so that $\mathbf{k} \cdot \boldsymbol{\epsilon} = 0$, $\epsilon^0 \epsilon^0 = 0$, and $\boldsymbol{\epsilon} \cdot \boldsymbol{\epsilon} = 1$. So the spectral photon production rate per transverse polarization degree of freedom is

$$\frac{d\dot{n}_\gamma}{d\omega} = n_Z n_e \frac{8 Z^2 \alpha^2}{3} \frac{\alpha}{\pi} \frac{\mathcal{S}(\omega)}{\omega}. \quad (4.11)$$

This quantity is directly related to the medium response function $\mathcal{S}(\omega)$. Therefore, we can express the neutrino emissivity of equation (4.9) in terms of the photon emissivity as

$$\begin{aligned} \frac{d\dot{n}_\nu}{d\omega_\nu} = \frac{G_F^2}{6\pi^3 \alpha} \int_{\omega_\nu}^{\infty} d\omega \left(\frac{d\dot{n}_\gamma}{d\omega} \right) \frac{\omega_\nu^2 (\omega - \omega_\nu)^2}{\omega^3} \\ \times \left[C_V^2 (3\omega^2 - 2\omega\omega_\nu + 2\omega_\nu^2) + 2C_A^2 (3\omega^2 - 5\omega\omega_\nu + 5\omega_\nu^2) \right]. \end{aligned} \quad (4.12)$$

Therefore, given the spectral photon emissivity, e.g. taken from the photon opacity calculation, we can directly extract the neutrino emission spectrum. We will return to this point in section 5.

Axions couple to the electron axial current with an interaction of the derivative form $(C_e/2f_a) \bar{\psi}_e \gamma^\mu \gamma_5 \psi_e \partial_\mu a$, where a is the axion field, f_a the axion decay constant, and C_e a model-dependent numerical coefficient. One often uses a dimensionless axion-electron

Yukawa coupling $g_{ae} = C_e m_e / f_a$ so that the interaction is $(g_{ae}/2m_e) \bar{\psi}_e \gamma^\mu \gamma_5 \psi_e \partial_\mu a$. The bremsstrahlung emission rate is found to be

$$\dot{n}_a = n_Z n_e \frac{8 Z^2 \alpha^2}{3} \int \frac{d^3 \mathbf{k}}{2\omega (2\pi)^3} \left(\frac{g_{ae}}{2m_e} \right)^2 \frac{\bar{M}_A^{\mu\nu} k_\mu k_\nu}{\omega^4} \mathcal{S}(\omega). \quad (4.13)$$

For massless axions with $\omega = |\mathbf{k}|$ we find for the contraction $\bar{M}_A^{\mu\nu} k_\mu k_\nu = 2\omega^4$. Therefore, the spectral emissivity is

$$\frac{d\dot{n}_a}{d\omega} = n_Z n_e \frac{8 Z^2 \alpha^2}{3} \left(\frac{g_{ae}}{2m_e} \right)^2 \frac{\omega}{2\pi^2} \mathcal{S}(\omega). \quad (4.14)$$

Notice that this spectrum is harder than the photon spectrum by a factor ω^2 caused by the derivative structure of the axion interaction. Still, fundamentally it depends on the same medium response function $\mathcal{S}(\omega)$. We have checked that in the nondegenerate limit this axion emission rate agrees with reference [32].

4.4 Medium response function and screening effects

The medium response function defined in equation (4.8) could be easily evaluated if the nuclei used as scattering centers were uncorrelated. However, their Coulomb interaction leads to anticorrelations encoded in an ion structure factor $S_i(\mathbf{q}^2)$ similar to the case of electron-electron correlations discussed in section 3.2. Therefore, under the integral in equation (4.8) we need to include $S_i(\mathbf{q}^2)$, which we will discuss later. We mention in passing that $\mathcal{S}(\omega)$ given in equation (4.8), with or without including $S_i(\mathbf{q}^2)$, fulfills the detailed-balancing condition $\mathcal{S}(-\omega) = \mathcal{S}(\omega) e^{\omega/T}$. Here a negative ω means energy absorbed by the medium, whereas a positive ω for us always means energy emitted, although in the literature one usually uses the opposite convention.

To write $\mathcal{S}(\omega)$ in a more compact form we first note that the electron number density is given by equation (3.6) in terms of the nonrelativistic degeneracy parameter η . We further write the kinetic electron energy in dimensionless form as $u = \mathbf{p}^2 / (2m_e T)$ so that the occupation number is $f_u = 1 / (e^{u-\eta} + 1)$. Then the structure function is

$$\mathcal{S}(\omega) = \frac{\pi}{m_e \sqrt{2m_e T}} s(\omega/T) \quad (4.15)$$

where

$$s(w) = \int_0^\infty du_2 \frac{\sqrt{u_1 u_2}}{e^{u_1 - \eta} + 1} \frac{1}{e^{-(u_2 - \eta)} + 1} \int_{-1}^{+1} dc_\theta \frac{2m_e T}{\mathbf{q}^2} S_i(\mathbf{q}^2) \Big/ \int_0^\infty du \frac{\sqrt{u}}{e^{u-\eta} + 1}. \quad (4.16)$$

Here $u_1 = u_2 + w$ and $w = \omega/T$. Moreover, $\mathbf{q}^2 = |\mathbf{p}_1 - \mathbf{p}_2|^2 = \mathbf{p}_1^2 + \mathbf{p}_2^2 - 2|\mathbf{p}_1||\mathbf{p}_2|c_\theta$ with $c_\theta = \cos \theta$. Therefore, $\mathbf{q}^2 / (2m_e T) = u_1 + u_2 - 2\sqrt{u_1 u_2} c_\theta$.

Besides the original squared matrix element, this function depends on electron degeneracy effects and Coulomb correlation effects encoded in $S_i(\mathbf{q}^2)$. Anticipating that electron degeneracy is not a large correction we first reduce this expression to Maxwell-Boltzmann rather than Fermi-Dirac statistics. Formally this is the $\eta \rightarrow -\infty$ limit, leading to the nondegenerate (ND) structure function

$$s_{\text{ND}}(w) = \int_0^\infty du e^{-u-w} \sqrt{(u+w)u} F_i(u, w) \Big/ \int_0^\infty du e^{-u} \sqrt{u}, \quad (4.17)$$

where the integral in the denominator is simply $\sqrt{\pi}/2$. The integral kernel is

$$F_i(u, w) = \int_{-1}^{+1} dc_\theta \frac{2m_e T S_i(\mathbf{q}^2)}{\mathbf{q}^2}. \quad (4.18)$$

The ion structure function from Coulomb correlation effects will be an expression of the type given in equation (3.7), but with the role of electrons and ions interchanged. However, in a multi-component plasma, an exact treatment is difficult; because screening will be a relatively small correction, we use

$$S_i(\mathbf{q}^2) = \frac{\mathbf{q}^2}{\mathbf{q}^2 + k_s^2}, \quad (4.19)$$

where k_s is a phenomenological screening scale. We use k_i given in equation (3.8) for the ion correlations. With $\mu = k_s^2/(2m_e T)$ we therefore use

$$\begin{aligned} F_i(u, w) &= \int_{-1}^{+1} dc_\theta \frac{1}{\mu + 2u + w - 2\sqrt{(u+w)u}c_\theta} \\ &= \frac{1}{2\sqrt{(u+w)u}} \log \left(\frac{\mu + 2u + w + 2\sqrt{(u+w)u}}{\mu + 2u + w - 2\sqrt{(u+w)u}} \right). \end{aligned} \quad (4.20)$$

Without screening ($\mu = 0$) this expression diverges logarithmically for small w . However, for axion emission and neutrino pair emission, this divergence is moderated by at least one power of ω , so even without correlation effects, the emission of soft radiation does not diverge. Near the solar center one finds $k_i = 7$ keV and with $T = 1.3$ keV one finds $\mu = 0.037 \ll 1$, so screening is not a strong effect. Overall then the ND structure function is

$$s_{\text{ND}}(w) = \frac{e^{-w}}{\sqrt{\pi}} \int_0^\infty du e^{-u} \log \left(\frac{\mu + 2u + w + 2\sqrt{(u+w)u}}{\mu + 2u + w - 2\sqrt{(u+w)u}} \right) \rightarrow \frac{2e^{-w}}{\sqrt{w}} \quad (\text{large } w) \quad (4.21)$$

In figure 12 we show $e^w s_{\text{ND}}(w)$ with and without Coulomb correlation effects and the asymptotic form for large w . We also show as a red line $e^w s(w)$ including Fermi-Dirac statistics for the electrons with $\eta = -1.4$, appropriate for the solar center.

While correlation effects strongly modify the structure function at low energy transfer, this effect is much smaller after folding with the neutrino phase space according to equation (4.9). Even without correlations, the neutrino spectrum does not diverge at low energies. Including Coulomb correlations reduces it at low energies by some 20% and only by very little in the main keV-range of the spectrum. Pauli blocking of final states provides a further 5% suppression effect at very low energies, so overall these are fairly minor effects.

4.5 Electron-electron bremsstrahlung

The electron-electron bremsstrahlung process is similar to electron-proton bremsstrahlung with a number of important modifications [32]. The vector-current emission rate is of higher order in velocity—the simple dipole term vanishes in the scattering of equal-mass particles. In the non-degenerate and non-relativistic limit and ignoring Coulomb correlations, the axial-vector rate is $1/\sqrt{2}$ that of the electron-proton rate. In other words, we obtain the ee bremsstrahlung rate from the axial-current part of equation (4.9) with the substitution $Z^2 n_Z n_e \rightarrow n_e^2/\sqrt{2}$.

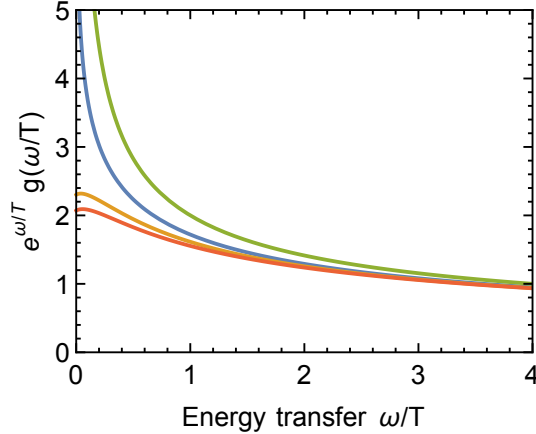


Figure 12. Structure function $e^w s(w)$ for bremsstrahlung. *Blue line:* Non-degenerate electrons given in equation (4.21) without Coulomb correlations ($\mu = 0$). *Orange line:* Coulomb correlations included with $\mu = 0.04$ appropriate for the solar center. *Red line:* Electron degeneracy included with $\eta = -1.4$ appropriate for the solar center. *Green line:* Asymptotic form for large $w = \omega/T$.

Taking degeneracy effects and Coulomb correlations exactly into account would be very hard. Instead we simply add the electron-electron term to the electron-ion one and therefore use the same treatment as for the latter. These corrections are rather small and ee bremsstrahlung is subdominant, so the overall error introduced by this approach is on the level of a few percent.

4.6 Solar neutrino flux

As a final step we integrate the bremsstrahlung emission rate over our standard solar model to obtain the neutrino flux at Earth. In figure 13 we show separately the vector and axial-vector contributions from electron-ion scattering as well as the one from electron-electron scattering which only contributes in the axial channel. These curves need to be multiplied

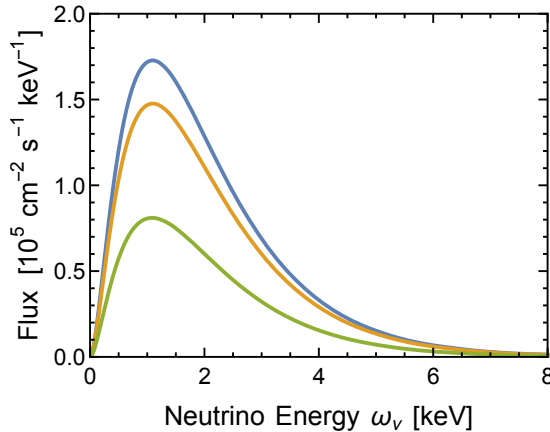


Figure 13. Neutrino flux from bremsstrahlung production for the vector (blue) and axial-vector (orange) electron-ion interaction, and from the ee interaction (green) which contributes only in the axial-vector channel. For the proper flux, the blue curve is to be multiplied with C_V^2 , the orange and green curves with $2C_A^2$.

with the flavor-dependent values of C_V^2 and $2C_A^2$ to obtain the proper fluxes. For the electron contributions, we include only hydrogen and helium as targets. The contribution from metals is only a few percent and will be included in the opacity-derived flux in section 5.

Finally we show in figure 14 the axial-channel bremsstrahlung flux for one flavor in comparison with the ν_e flux from the nuclear pp reaction and from T plasmon decay. Similar to the Compton process, the bremsstrahlung flux becomes important in the cross-over region between the T-plasmon and pp fluxes.

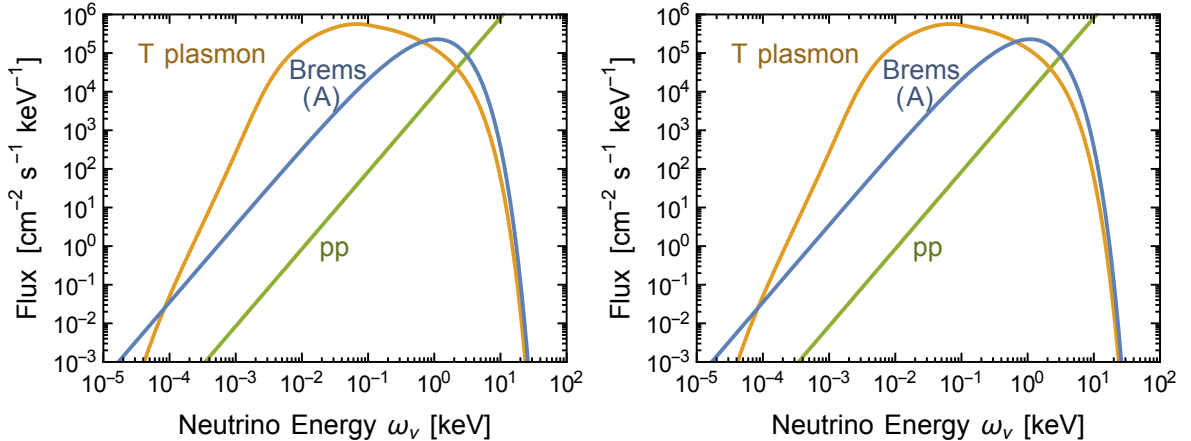


Figure 14. Solar neutrino flux at Earth from the axial-channel bremsstrahlung process (eI and ee contributions) for one flavor, compared with the pp flux (only ν_e) and transverse plasmon decay (ν_e and equal flux $\bar{\nu}_e$). Flavor oscillations are not considered here.

Bremsstrahlung is the dominant contribution at very low energies. From equation (4.9) we see that for very low neutrino energies, the spectrum varies as ω_ν^2 , independently of details of the structure function $\mathcal{S}(\omega)$. This scaling remains true after integrating over the Sun, so the very-low energy thermal emission spectrum scales as ω_ν^2 and thus in the same way as the pp flux given in equation (2.18).

4.7 Beyond the Born approximation

Traditionally the bremsstrahlung emission rate of neutrinos and other particles is calculated in Born approximation starting with the usual Feynman rules. However, the bremsstrahlung emission by a non-relativistic electron scattering on an ion receives a significant modification if one uses appropriately modified electron wave functions instead of plane waves, a point first discussed in the context of x-ray production in free-free transitions a long time ago by Sommerfeld [35]. Such an enhancement in bremsstrahlung emission arises because of the long-range Coulomb potential. It is the counterpart of what is known as Fermi-Coulomb function in the context of beta decay and of the so-called Sommerfeld enhancement, to be taken into account in dark matter annihilation processes [36]. In these cases, the correction is simply given by $f(v) = |\psi(0)|^2$, i.e., by the normalization of the outgoing (or ingoing) Coulomb distorted wave function

$$\sigma = \sigma_0 f(v) = \sigma_0 \frac{2\pi Z\alpha}{v} \frac{1}{1 - e^{-\frac{2\pi Z\alpha}{v}}}, \quad (4.22)$$

where σ_0 is the cross section evaluated with plane waves and v is the velocity of the outgoing (or ingoing) particle.

Such corrections have been extensively studied also for bremsstrahlung (see e.g. reference [37]). Elwert found that a good approximation to correct the Born scattering formula is obtained by simply multiplying equation (4.8) by the factor [38]

$$f_E = \frac{v_i}{v_f} \frac{1 - e^{-\frac{2\pi Z\alpha}{v_i}}}{1 - e^{-\frac{2\pi Z\alpha}{v_f}}}, \quad (4.23)$$

which is the ratio $|\psi_f(0)|^2/|\psi_i(0)|^2$ of the final and initial state electron wave functions. In figure 15 (green line) we show the effect on the overall solar neutrino flux of including this factor in the bremsstrahlung rate, leading to a typical 20–30% enhancement. We also show as an orange line the effect of including Coulomb correlations which reduce the flux typically by some 5%. At very small energies, the Elwert factor becomes less important and Coulomb correlations more important.

As noted by one of us in the context of solar axion emission [13], the Sommerfeld correction is included in the photon opacity calculation. On the other hand, using unscreened Coulomb wave functions in a stellar plasma is not fully consistent—the true correction should be considerably smaller, especially for bremsstrahlung on hydrogen and helium. Therefore,

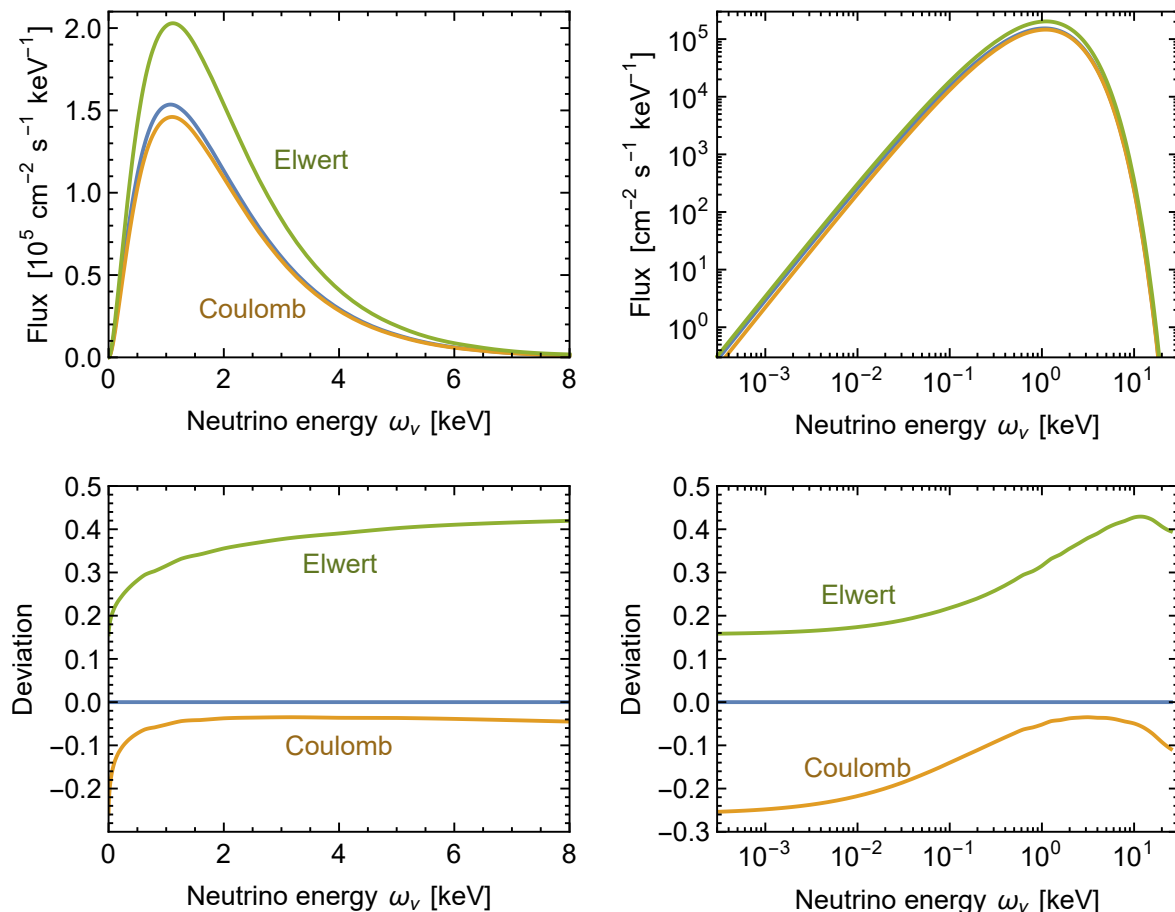


Figure 15. Solar neutrino flux from bremsstrahlung production for axial-vector electron-ion interaction, without corrections (blue), and including respectively correlations (orange) and the Elwert factor (green). For the proper flux, the curves in the upper panels are to be multiplied with $2C_A^2$.

as in reference [13] we calculate these rates directly, not from the opacities, and leave out the Elwert factor, possibly underestimating the true flux by some 10%. On the other hand, we will include the Coulomb correlation factor. At keV-range energies this makes no big difference, but should be a reasonable correction in the far sub-keV range where bremsstrahlung is the dominant flux and the Elwert factor is small.

5 Free-bound and bound-bound transitions

The nuclei of the solar plasma are imperfectly ionized, notably the “metals” (elements heavier than helium). Therefore, in addition to bremsstrahlung (free-free electron transitions), free-bound (fb) and bound-bound (bb) transitions are also important for particle emission. In the context of axion emission by electrons, these processes imprint a distinctive line pattern on the expected solar axion flux [13]. Likewise, the photon opacities, as input to solar models, depend strongly on these processes. In reference [8] free-bound processes were included by explicit atomic transition calculations for a number of elements.

However, following the approach taken by one of us in an earlier paper for calculating the solar axion flux [13], the emission rate can be related to the photon opacity by equation (4.12), i.e., the neutrino emissivity is the same as the phase-space weighted photon emissivity. Therefore, one can use the solar photon opacity from the literature to derive the neutrino emissivity. In section 4.3 we have derived the relation between photon and neutrino emissivity explicitly for bremsstrahlung, but it applies in this form to all processes where a nonrelativistic electron makes a transition in the potential of an external scattering center which takes up momentum. In other words, it applies in the long-wavelength approximation with regard to the electron. On the other hand, this relation does not apply to electron-electron bremsstrahlung, the Compton process, or plasmon decay.

While we could have used this relation to extract the bremsstrahlung emissivity from the opacities, we have preferred to treat bremsstrahlung on hydrogen and helium as well as electron-electron bremsstrahlung explicitly in the interest of completeness. For the fb

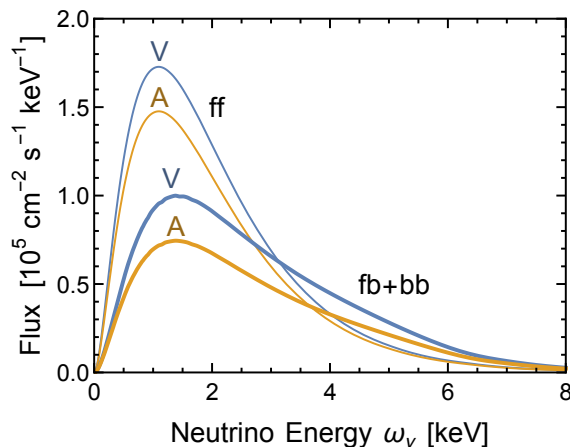


Figure 16. Solar neutrino flux at Earth from free-free (ff), free-bound (fb) and bound-bound (bb) electron-ion transitions for the vector (V) and axial-vector (A) contributions. The proper fluxes are found by multiplying the curves with C_V^2 and $2C_A^2$, respectively. The ff curves include bremsstrahlung on hydrogen and helium and are the same as in figure 13; they exclude electron-electron bremsstrahlung. The fb+bb curves include bremsstrahlung on metals.

and bb transitions as well as bremsstrahlung on metals we proceed as in reference [13] to extract the neutrino emissivity. In figure 16 we show the resulting neutrino flux spectrum at Earth in comparison with the bremsstrahlung result on hydrogen and helium derived earlier. We show the vector and axial-vector contributions, each to be multiplied with the flavor-dependent C_V^2 or $2C_A^2$ to arrive at the proper flux. While the fb and bb contributions are subdominant relative to bremsstrahlung, they dominate at higher energies. This behavior was to be expected because they are more relevant than ff processes in the Rosseland opacities at any radius (see e.g. figure 15 of reference [39]).

6 Solar neutrino flux at Earth

6.1 Flavor-dependent fluxes

In order to consolidate the solar flux results from different thermal processes we show the spectra at Earth in figure 17. In the left panel we show all contributions relevant for the vector coupling, where the true flux is found by multiplication with the flavor-dependent value of C_V^2 . At low energies, plasmon decay dominates, at intermediate ones bremsstrahlung, and at the highest energies Compton process. In the right panel we show the analogous axial-vector result which does not have any significant plasmon-decay contribution.

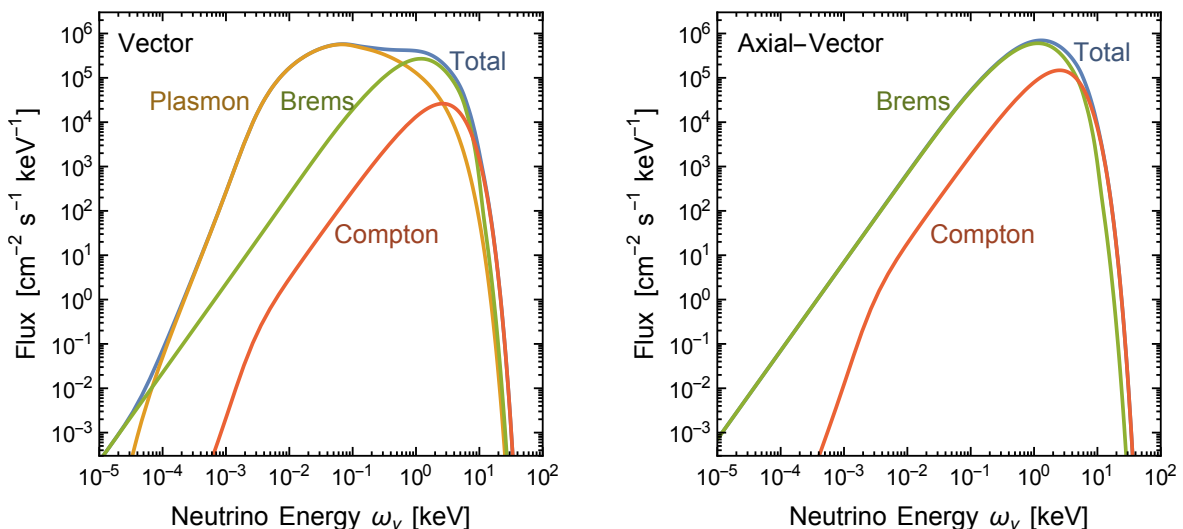


Figure 17. Solar neutrino flux at Earth from the indicated processes, where “brems” includes ff, fb and bb. *Left panel:* Vector coupling, for proper flux multiply with C_V^2 . *Right panel:* Axial-vector coupling, for proper flux multiply with C_A^2 .

The intrinsic uncertainties of the various emissivity calculations should not be larger than a few tens of percent concerning various issues of in-medium effects such as correlations or Coulomb wave functions of charged particles. In addition, every process has a different dependence on temperature, density and chemical composition so that different standard solar models will produce somewhat different relative weights of the different processes. We have not studied the variation of the different flux contributions depending on different standard solar models, but the overall uncertainty again should be in the general ten percent range.

We may show the same results in a somewhat different form if we observe that the vector-current processes produce almost exclusively $\nu_e \bar{\nu}_e$ pairs, whereas the axial-vector processes

produce all flavors in equal measure. In the upper panels of figure 18 we show these total fluxes, where now the coupling constants $C_V^2 = 0.9263$ and $C_A^2 = 1/4$ are included. In addition we show the ν_e flux from the nuclear pp reaction. In the bottom panels we add the different source channels for every flavor and show the keV-range fluxes for ν_e , $\bar{\nu}_e$, and each of the other species, still ignoring flavor oscillations.

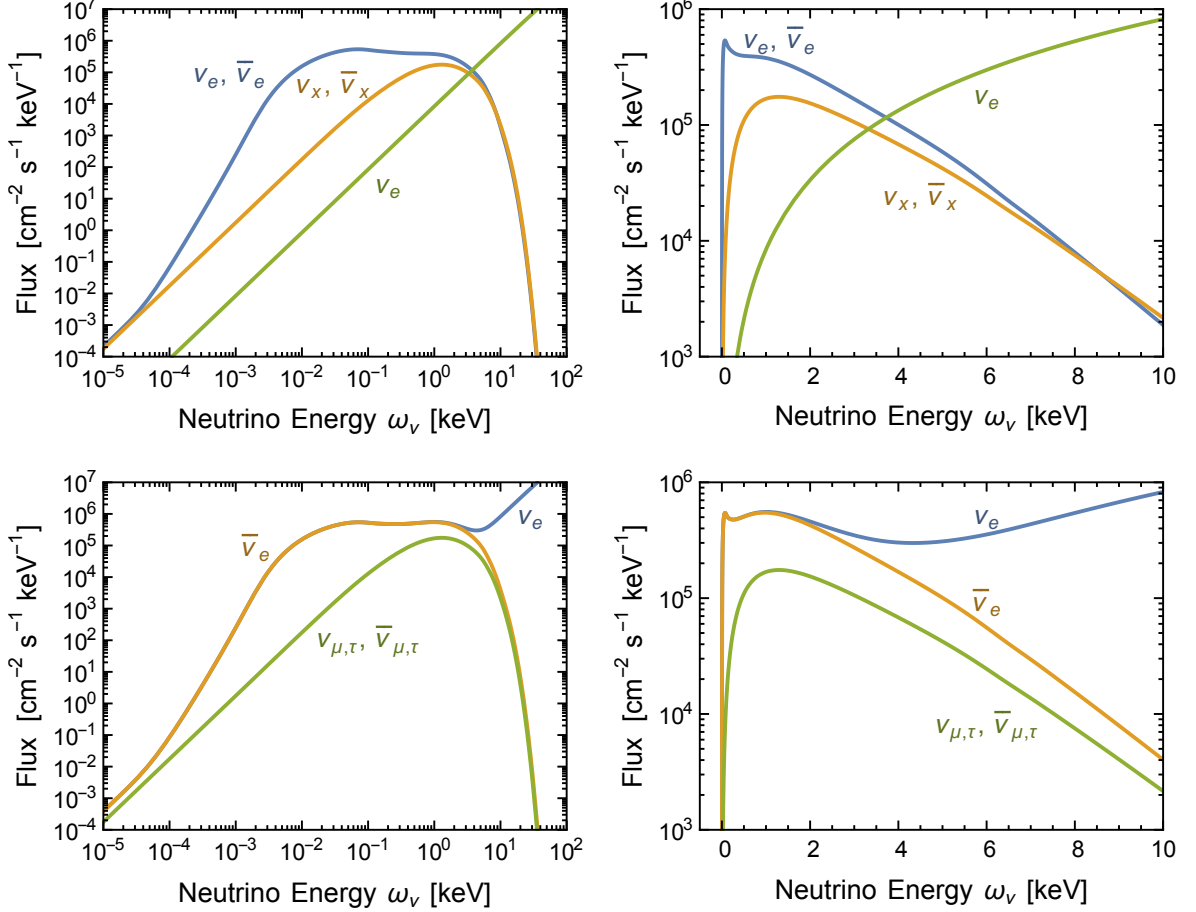


Figure 18. Flavor-dependent solar neutrino fluxes at Earth, ignoring flavor mixing. *Top panels:* Thermal flux from vector-current interactions producing only $\nu_e\bar{\nu}_e$ pairs, axial-vector emission, producing equal fluxes of every flavor, where x stands for e , μ or τ , and ν_e from the nuclear pp reaction. *Bottom panels:* ν_e , $\bar{\nu}_e$, and other single-species fluxes after adding the source channels.

6.2 Including flavor mixing

Flavor-eigenstate neutrinos are mixtures of three different mass eigenstates. After propagating over a long distance, these mass eigenstates effectively decohere, so the neutrino flux arriving at Earth is best described as an incoherent mixture of mass eigenstates. It depends on the nature of a possible detector if these should be re-projected on interaction eigenstates or if these fluxes can be used directly if the detection channel is flavor blind. As we do not know the nature of such a future detector, the neutrino flux in terms of mass eigenstates is the most natural form of presentation.

The axial-current production channel has amplitude $C_A = +1/2$ for ν_e and $C_A = -1/2$ for the other flavors, yet on the level of the rate (proportional to C_A^2) all flavors are produced

in equal measure. Therefore, the density matrix in flavor space is proportional to the 3×3 unit matrix and thus the same in any basis. Without further ado we can think of the axial-current processes as producing mass eigenstates, so in the upper panels of figure 18, the fluxes marked ν_x and $\bar{\nu}_x$ can be interpreted as x standing for the mass indices 1, 2 and 3.

The vector-current channels, on the other hand, have the peculiar property of producing almost exclusively e -flavored states as discussed earlier, which is also true of the charged-current pp nuclear reaction. These states oscillate in flavor space after production. The relevant oscillation scale is $\omega_{\text{osc}} = \Delta m^2 / 2E = 3.8 \times 10^{-8} \text{ eV} / E_{\text{keV}}$ for the solar mass difference of $\Delta m^2 = 7.5 \times 10^{-5} \text{ eV}^2$ and using $E_{\text{keV}} = E / \text{keV}$. For the atmospheric mass difference $\Delta m^2 = 2.5 \times 10^{-3} \text{ eV}^2$ the oscillation scale is $\omega_{\text{osc}} = 1.25 \times 10^{-3} \text{ eV} / E_{\text{keV}}$. These numbers should be compared with the matter-induced energy splitting between ν_e and the other flavors of $\Delta V = \sqrt{2} G_{\text{F}} n_e = 7.6 \times 10^{-12} \text{ eV}$ for the electron density $n_e = 6 \times 10^{25} \text{ cm}^{-3}$ of the solar center. Therefore, for keV-range neutrinos, the matter effect is very small and neutrino oscillations proceed essentially as in vacuum. The source region in the Sun is much larger than the oscillation length and is far away from Earth, so flavor oscillations effectively decohere long before reaching here. Therefore, we may think of the e -flavored channels as producing an incoherent mixture of mass eigenstates. On the probability level, the best-fit mass components of ν_e are [40]

$$p_1 = 67.9\%, \quad p_2 = 29.9\%, \quad p_3 = 2.2\%. \quad (6.1)$$

On this level of precision, these probabilities do not depend on the mass ordering. The final fluxes in terms of mass eigenstates were shown in figure 2 in the introduction as our main result.

7 Discussion and summary

We have calculated the solar neutrino flux produced by various thermal processes that produce $\nu\bar{\nu}$ pairs with keV-range energies. A proposed dark matter detector for keV-mass sterile neutrinos might find this flux to be a limiting background and conversely, conceivably it could measure this solar flux, although these are somewhat futuristic ideas. Whatever these experimental developments, it is well motivated to provide a benchmark calculation of the thermal solar neutrino flux.

One complication is that there is not a single dominant production channel, but all the processes shown in figure 1 are relevant in different ranges of energy. Each of them has its own idiosyncratic issues concerning in-medium many-body effects, yet we think that our flux calculations should be correct on the general 10% level of precision. Similar uncertainties arise from the variation between different standard solar models. The only previous study of the keV-range solar neutrino flux in reference [8] stressed the importance of a plasmon enhancement in the photo-production channel, but we think that this result is spurious as argued in section 2.5 and we think that this particular collective effect is not relevant.

It is interesting that the free-bound and bound-bound emission processes on elements heavier than hydrogen and helium produce the dominant flux in the few-keV range. We have calculated this flux taking advantage of the solar opacity calculations available in the literature. The neutrino emissivity is related by a simple phase-space integration to the monochromatic photon emissivity provided by the opacity calculations. Our solar flux based on these processes roughly agrees with that of reference [8] who estimated it by direct calculation on several characteristic elements. Therefore, this flux carries information about

the solar metal abundances, quantities of crucial interest in the context of the “solar opacity problem,” a point stressed in reference [8]. As this flux is no longer overshadowed by the spurious plasmon resonance in the photo-production channel, this argument is resurrected by our study, i.e., a measurement of the keV-range flux could provide nontrivial information on the solar metal content.

Acknowledgments

We thank Thierry Lasserre for bringing up the question of the low-energy solar neutrino flux, and Alexander Millar for helpful discussions. In Munich, we acknowledge partial support by the Deutsche Forschungsgemeinschaft through Grant No. EXC 153 (Excellence Cluster “Universe”) and Grant No. SFB 1258 (Collaborative Research Center “Neutrinos, Dark Matter, Messengers”) as well as by the European Union through Grant No. H2020-MSCA-ITN-2015/674896 (Innovative Training Network “Elusives”). J.R. is supported by the Ramon y Cajal Fellowship 2012-10597 and FPA2015-65745-P (MINECO/FEDER).

A Standard solar model

In the main text we show neutrino fluxes produced from integration over the solar volume. The neutrino production rates are nontrivial functions of several parameters (temperature, density, mass-fraction of each species) which depend on the radial position in the Sun and determine the local plasma properties. These radial profiles of temperature, density, etc. are not directly measured; rather, they are obtained from a solar model. The latter is a theoretical description of the Sun, obtained by evolving certain initial conditions (mass, helium and metal abundances) through a stellar evolution code, which in turn depends on radiative opacities, the treatment of convection, and so forth, to fit the present-day radius, luminosity, and photospheric composition. The latter is the one present-day boundary condition about which estimations vary the most.

In principle, consistency would require us to use a specific solar model for all processes; this should be a solar model obtained using the opacity code and the abundances exploited for the neutrino bremsstrahlung emission calculation. However, the differences between different solar models are small, introducing uncertainties in the neutrino emissivity on the order of 10% perhaps, so we can use more practical criteria for our calculations. First, we want to use a solar model that not only covers in detail the central core but also the external layers because they rule the low energy flux from T-plasmon decay.³ The Saclay solar model [44, 45] is, in this regard, the most complete one known to us. This model has the additional interest that it was built to reproduce the sound-speed profile (to a large extent due to the temperature profile) measured by helioseismology by adjusting some parameters (like initial metallicity, opacities) which are not directly measurable. The model used was built when the surface chemical composition GS98 [42] was suitable to reproduce the helioseismology data with very minor adjustments.

The recent revision of the surface chemical composition AGSS09 [43] led to a downward adjustment of abundances, mostly CNO, Ne and refractories, providing a lower opacity and thus some tension between solar models and helioseismology. This tension has led to a large number of publications but is largely irrelevant for the level of precision that we must assume

³Note however that the latter is subdominant to the bremsstrahlung neutrinos, which are mostly produced in the core.

in our calculations. The difference between GS98 and AGSS09 abundances is 20–40% in CNO and $\sim 12\%$ in refractories; both are obtained from spectroscopic observations together with hydrodynamical simulations. We emphasize that the first one agrees with the helioseismic measurements, whereas the second one (which is a more accurate 3D simulation) does not, see reference [47] for a recent discussion. This situation constitutes the so-called solar abundance problem. Differences in sound speed profiles (temperatures) are however only around 1%.

We prefer to use the GS98 surface composition as it fits better the solar internal structure. The radial profile of the abundance of several chemical elements is not specified in the Saclay model, so we use instead the abundance profiles of the GS98 model of reference [46]. The profiles of temperature, electron density, plasma frequency, degeneracy parameter η , Pauli blocking factor, and screening scales for our solar model choice are displayed in the following figures.

On the other hand, by far the most detailed monochromatic opacities publicly available are those of the Opacity Project [41], which are tabulated for different metals and can thus be combined for different solar compositions. For this reason, they were used in reference [13] to compute the axion emission in free-bound and bound-bound transitions. In the same study, three different opacity codes were compared with excellent agreement. Therefore we have used the OP opacities for our calculations in this paper.

In figures 19–22 we show the radial variation of various characteristic parameters of our standard solar model. In figure 23 we show the region of origin of the thermal solar neutrinos calculated in the main text. The left panel shows that most of the flux originates within $0.2 R_\odot$ with a maximum around $0.1 R_\odot$. Notice that emission near the solar center is suppressed by the small volume of this region, i.e., by the geometric r^2 factor. In the right panel, we show the same information, but for each neutrino energy, the flux is normalized to 1. For smaller neutrino energies, the production site is somewhat shifted to larger solar radii.

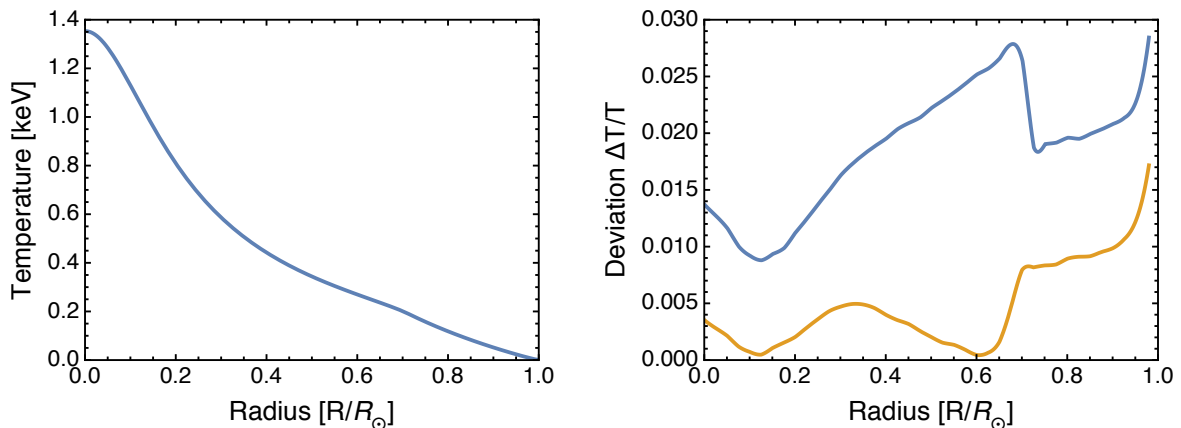


Figure 19. Temperature profile. *Left panel:* Saclay model [44, 45], our standard case. *Right panel:* Relative deviations between solar models. *Blue line:* Saclay model vs. model [46] with AGSS09 abundances. *Orange line:* Saclay model vs. model [46] with GS98 abundances.

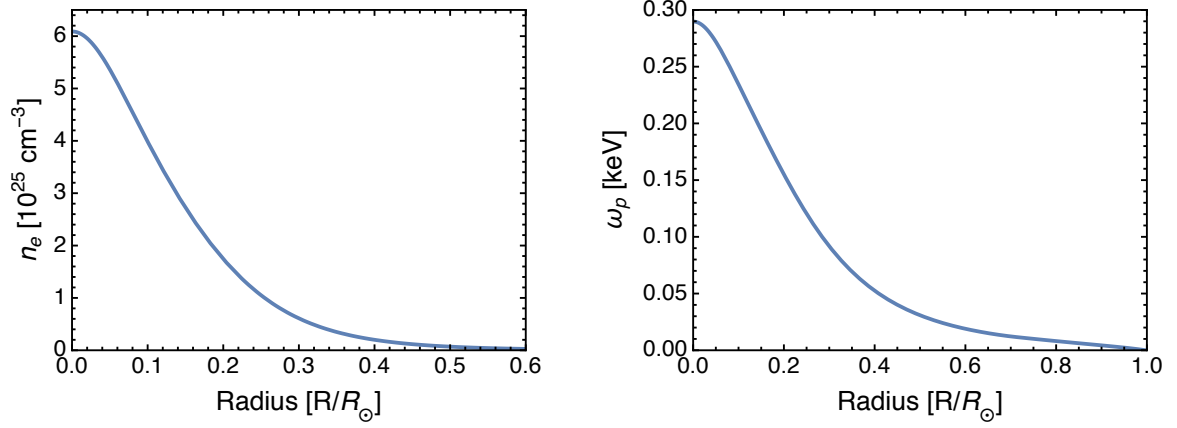


Figure 20. *Left panel:* Electron number density. *Right panel:* Plasma frequency.

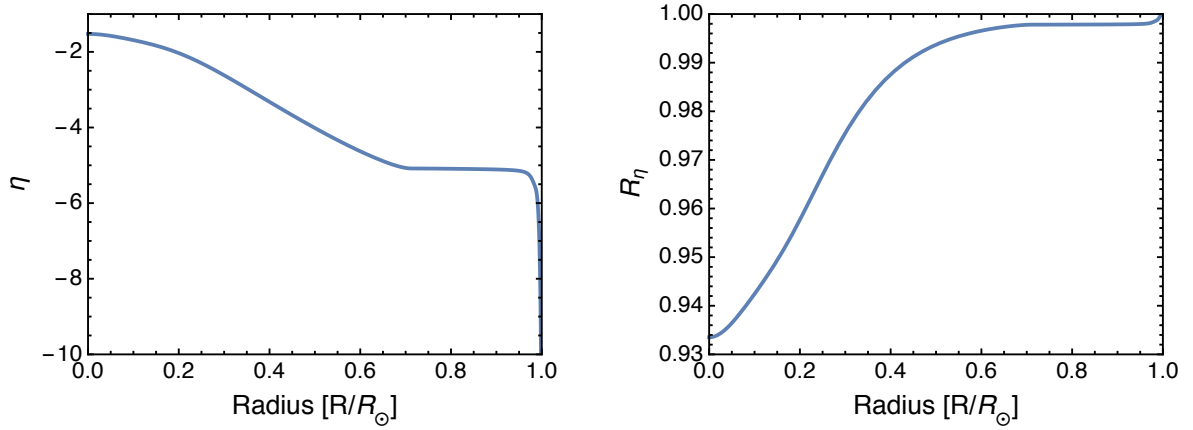


Figure 21. *Left panel:* Nonrelativistic degeneracy parameter η , where $\eta \rightarrow -\infty$ corresponds to a Maxwell-Boltzmann distribution. *Right panel:* Average Pauli blocking factor when electron recoils are small.

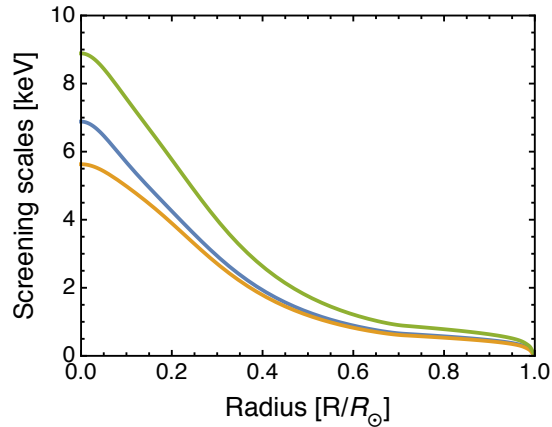


Figure 22. Phenomenological screening scales. *Orange line:* Electron screening k_e . *Blue line:* Ion screening k_i . *Green line:* Total Debye scale k_s .

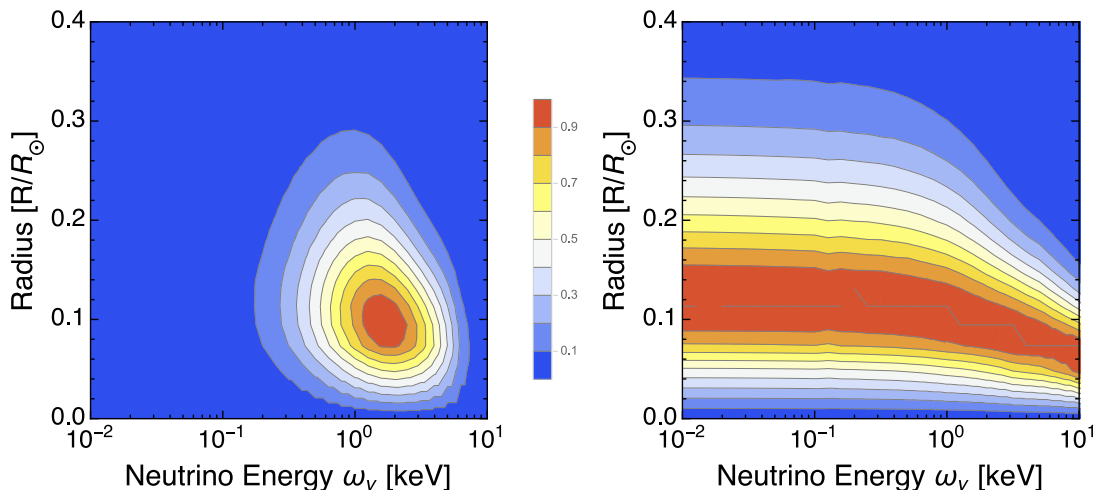


Figure 23. Isocontours of thermal neutrino emission. *Left panel:* The total flux (including the geometrical r^2 factor) is normalized to 1. *Right panel:* For each neutrino energy, the flux is normalized to 1. The production site of very low energy neutrinos is displaced towards the solar surface, but only slightly.

References

- [1] M. Drewes et al., *A white paper on keV sterile neutrino dark matter*, JCAP **1701** (2017) 025 [arXiv:1602.04816].
- [2] T. Lasserre, K. Altenmueller, M. Cribier, A. Merle, S. Mertens and M. Vivier, *Direct search for keV sterile neutrino dark matter with a stable dysprosium target*, arXiv:1609.04671.
- [3] Y. F. Li and Zhi-zhong Xing, *Possible capture of keV sterile neutrino dark matter on radioactive β -decaying nuclei*, Phys. Lett. B **695** (2011) 205 [arXiv:1009.5870].
- [4] Y. F. Li and Zhi-zhong Xing, *Captures of hot and warm sterile antineutrino dark matter on EC-decaying ^{163}Ho nuclei*, JCAP **1108** (2011) 006 [arXiv:1104.4000].
- [5] S. Ando and A. Kusenko, *Interactions of keV sterile neutrinos with matter*, Phys. Rev. D **81** (2010) 113006 [arXiv:1001.5273].
- [6] M. D. Campos and W. Rodejohann, *Testing keV sterile neutrino dark matter in future direct detection experiments*, Phys. Rev. D **94** (2016) no.9, 095010 [arXiv:1605.02918].
- [7] C. Spiering, *Towards high-energy neutrino astronomy—a historical review*, Eur. Phys. J. H **37** (2012) 515 [arXiv:1207.4952].
- [8] W. C. Haxton and W. Lin, *The very low energy solar flux of electron and heavy-flavor neutrinos and antineutrinos*, Phys. Lett. B **486** (2000) 263 [nucl-th/0006055].
- [9] M. Pospelov, A. Ritz and M. B. Voloshin, *Bosonic super-WIMPs as keV-scale dark matter*, Phys. Rev. D **78** (2008) 115012 [arXiv:0807.3279].
- [10] A. Derevianko, V. A. Dzuba, V. V. Flambaum and M. Pospelov, *Axio-electric effect*, Phys. Rev. D **82** (2010) 065006 [arXiv:1007.1833].
- [11] H. An, M. Pospelov and J. Pradler, *New stellar constraints on dark photons*, Phys. Lett. B **725** (2013) 190 [arXiv:1302.3884].
- [12] J. Redondo and G. Raffelt, *Solar constraints on hidden photons re-visited*, JCAP **1308** (2013) 034 [arXiv:1305.2920].

- [13] J. Redondo, *Solar axion flux from the axion-electron coupling*, JCAP **1312** (2013) 008 [arXiv:1310.0823].
- [14] E. Hardy and R. Lasenby, *Stellar cooling bounds on new light particles: Plasma mixing effects*, JHEP **1702** (2017) 033 [arXiv:1611.05852].
- [15] N. Itoh, H. Hayashi, A. Nishikawa, Y. Kohyama, *Neutrino Energy Loss in Stellar Interiors. VII. Pair, Photo-, Plasma, Bremsstrahlung, and Recombination Neutrino Processes*, Astrophys. J. Suppl. **102** (1996) 411.
- [16] C. J. Horowitz, *Weak magnetism for anti-neutrinos in supernovae*, Phys. Rev. D **65** (2002) 043001 [astro-ph/0109209].
- [17] J. B. Adams, M. A. Ruderman and C.-H. Woo, *Neutrino pair emission by a stellar plasma*, Phys. Rev. **129** (1963) 1383.
- [18] M. H. Zaidi, *Emission of neutrino-pairs from a stellar plasma*, Nuovo Cim. A **40** (1965) 502.
- [19] E. Braaten and D. Segel, *Neutrino energy loss from the plasma process at all temperatures and densities*, Phys. Rev. D **48** (1993) 1478 [hep-ph/9302213].
- [20] M. Haft, G. Raffelt and A. Weiss, *Standard and nonstandard plasma neutrino emission revisited*, Astrophys. J. **425** (1994) 222; Erratum *ibid.* **438** (1995) 1017 [astro-ph/9309014].
- [21] S. Ratkovic, S. I. Dutta and M. Prakash, *Differential neutrino rates and emissivities from the plasma process in astrophysical systems*, Phys. Rev. C **67** (2003) 123002 [astro-ph/0303501].
- [22] J. N. Bahcall, *Gallium solar neutrino experiments: Absorption cross-sections, neutrino spectra, and predicted event rates*, Phys. Rev. C **56** (1997) 3391 [hep-ph/9710491].
- [23] V. I. Ritus, *Photoproduction of neutrinos of electrons and the neutrino radiation from stars*, Sov. Phys. JETP **14** (1961) 915.
- [24] H. Y. Chiu and R. C. Stabler, *Emission of photoneutrinos and pair annihilation neutrinos from stars*, Phys. Rev. **122** (1961) 1317.
- [25] V. Petrosian, G. Beaudet and E. E. Salpeter, *Photoneutrino energy loss rates*, Phys. Rev. **154** (1967) 1445.
- [26] S. I. Dutta, S. Ratkovic and M. Prakash, *The photo-neutrino process in astrophysical systems*, Phys. Rev. D **69** (2004) 023005 [astro-ph/0309564].
- [27] D. B. Boercker, *Collective effects on Thomson scattering in the solar interior*, Astrophys. J. **316** (1987) L95.
- [28] P. Cazzola, G. De Zotti and A. Saggion, *Electron-nucleus neutrino bremsstrahlung*, Phys. Rev. D **3** (1971) 1722.
- [29] D. A. Dicus, E. W. Kolb, D. N. Schramm and D. L. Tubbs, *Neutrino pair bremsstrahlung including neutral current effects*, Astrophys. J. **210** (1976) 481.
- [30] G. M. Gandelman and V. S. Pinaev, *Emission of neutrino pairs by electrons and the role played by it in stars*, Zh. Eksp. Teor. Fiz. **37** (1960) 1072.
- [31] G. Guo and Y.-Z. Qian, *Spectra and rates of bremsstrahlung neutrino emission in stars*, Phys. Rev. D **94** (2016) 043005 [arXiv:1608.02852].
- [32] G. G. Raffelt, *Astrophysical axion bounds diminished by screening effects*, Phys. Rev. D **33** (1986) 897.
- [33] L. M. Krauss, J. E. Moody and F. Wilczek, *A stellar energy loss mechanism involving axions*, Phys. Lett. B **144** (1984) 391.
- [34] G. G. Raffelt, *Plasmon decay into low mass bosons in stars*, Phys. Rev. D **37** (1988) 1356.
- [35] A. Sommerfeld, *Über die Beugung und Bremsung der Elektronen*, Ann. Phys. **403** (1931) 257.

- [36] N. Arkani-Hamed, D. P. Finkbeiner, T. R. Slatyer and N. Weiner, *A theory of dark matter*, Phys. Rev. D **79** (2009) 015014 [arXiv:0810.0713].
- [37] W. J. Karzas and R. Latter, *Electron radiative transitions in a Coulomb field*, Astrophys. J. Suppl. **6** (1961) 167.
- [38] G. Elwert, *Verschärfte Berechnung von Intensität und Polarisation im kontinuierlichen Röntgenspektrum*, Ann. Phys. **426** (1939) 178.
- [39] M. Krief, A. Feigel and D. Gazit, *Solar opacity calculations using the super-transition-array method*, Astrophys. J. **821** (2016) 45 [arXiv:1601.01930].
- [40] I. Esteban, M. C. Gonzalez-Garcia, M. Maltoni, I. Martinez-Soler and T. Schwetz, *Updated fit to three neutrino mixing: Exploring the accelerator-reactor complementarity*, JHEP **1701** (2017) 087 [arXiv:1611.01514].
- [41] <http://cdsweb.u-strasbg.fr/topbase/>
- [42] N. Grevesse and A. J. Sauval, *Standard Solar Composition*, Space Sci. Rev. **85** (1998) 161.
- [43] M. Asplund, N. Grevesse, A. J. Sauval and P. Scott, *The chemical composition of the Sun*, Ann. Rev. Astron. Astrophys. **47** (2009) 481 [arXiv:0909.0948].
- [44] S. Turck-Chièze et al., *Solar neutrino emission deduced from a seismic model*, Astrophys. J. **555** (2001) L69.
- [45] S. Couvidat, S. Turck-Chièze and A. G. Kosovichev, *Solar seismic models and the neutrino predictions*, Astrophys. J. **599** (2003) 1434 [astro-ph/0203107].
- [46] A. Serenelli, S. Basu, J. W. Ferguson and M. Asplund, *New solar composition: The problem with solar models revisited*, Astrophys. J. **705** (2009) L123 [arXiv:0909.2668].
- [47] N. Vinyoles et al., *A new generation of standard solar models*, Astrophys. J. **835** (2017) 202 [arXiv:1611.09867].